TAMPEREEN TEKNILLINEN YLIOPISTO
TAMPERE UNIVERSITY OF TECHNOLOGY

NKETIAH GABRIEL

COMPARISON OF 2D AND 3D MRI TEXTURE ANALYSES OF FUNCTIONALLY DIFFERENT HIP MUSCLES

Master of Science Thesis

Supervisors: Professor Hannu Eskola
Sami J. Savio (MSc.)
Subject and supervisors approved by the Faculty Council of the Faculty of Natural Sciences on January 9, 2013

ABSTRACT

TAMPERE UNIVERSITY OF TECHNOLOGY
Master's Degree Programme in Biomedical Engineering
NKETIAH GABRIEL: Comparison of 2D and 3D MRI Texture Analyses of Functionally Different Hip Muscles
Master of Science Thesis, 64 pages, 1 Appendix page
January, 2013
Major subject: Medical Physics
Examiner: Professor Hannu Eskola
Keywords: Texture analysis (TA), Magnetic Resonance Imaging (MRI), skeletal muscles, hip, exercise-loading, two-dimensional (2D), three-dimensional (3D)

The need for detailed image information to enhance radiological decision making has necessitated computerized analysis of medical images. The superior sensitivity of MRI in detecting subtle changes in soft tissues has facilitated automatic analysis of MR images through texture analysis. Though there have been a number of recent studies in this area, most of them have focused on using 2D MRI texture analysis in detecting and classifying pathological tissues from healthy ones.

The objective of this thesis it to examine whether textural differences exist in hip muscles due to exercise-loading differences, if so, the effectiveness of 2D and 3D MRI texture analyses in detecting and characterizing these differences will be examined.

Ninety-one high-level female athletes representing five distinct loading sports (High-impact, odd-impact, high-magnitude, low-impact and non-impact exercise-loading) and 20 healthy non-athlete (referent) female subjects were used in this study. A 1.5T MRI scanner (Siemens, Erlangen, Germany) was used to acquire axial T1-weighted FLASH sequence images of the hip muscles. Two-dimensional(2D) and three-dimensional(3D) texture analyses were performed on four specific load-bearing muscles (gluteus maximus, gluteus medius, iliopsoas and obturator internus) using texture analysis application software – MaZda (TUL, Poland: COST Action B11). The computed texture parameters were statistically analyzed (using SPSS, Chicago, Ill.) to ascertain differences in texture between the four muscles, the non-athlete group and the athlete groups, and to characterize them accordingly. A comparative evaluation of 2D and 3D texture analyses was also made.

Significant differences (p-value < 0.00833) in texture were recorded between the four muscles. All the four muscles were found to be linearly separable from each other. Moreover, muscle texture of athletes who were involved in high-impact (triple-jumpers and high-jumpers), odd-impact (soccer and squash players) and low-impact (endurance runners) exercise-loadings differed significantly (p-value < 0.01) from that of the non-athletes. Subsequently, the high-impact, odd-impact and low-impact exercise-loading groups were completely separable from the non-athlete group. Contrarily, muscle texture of the high-magnitude (power lifters) and non-impact (swimmers) exercise-loading groups were not found to differ significantly from the non-athletes, some level of overlap was noticed in their classification from the non-athletes. Finally, 3D texture analysis was more effective in detecting and characterizing textural differences in skeletal muscles than the 2D texture analysis.

In conclusion, the 3D texture analysis of MR images provides a more accurate quantitative method for detecting and classifying textural differences in skeletal muscles that are associated with specific exercise-loading types.

PREFACE

The work presented in this thesis was carried out at the Department of Radiology, Medical Imaging Centre, Tampere University Hospital, Tampere, Finland, in cooperation with the Department of Biomedical Engineering, Tampere University of Technology, Tampere, Finland, and the UKK Institute for Health Promotion Research from June to December, 2012.

First and foremost, my sincerest gratitude and thanks goes to God, the Almightfy for His fervent love and favor. I would aslo like to express my profound gratitude to my supervisors, proferssor Hannu Eskola and Sami Savio (Msc.) for their time and guidance, and for the job opportunity they offered me.

I am most grateful to Prasun Dastidar (MD PhD) for his invaluable time and support in making all the necessary arrengements needed throughout this thesis.

Additinally, I want to specially thank Docent Harri Sievänen (ScD) and Riku Nikander (PhD) for their assistance in proving the data and discussing the biomechanical aspects of this study. I am also thanksful to Kirsi Holli (Msc PhD) and Paruthi Pradhapan (BEng) for their expertise advice and help.

Furthermore, I want to express my greatest thanks to all my family and friends for their continuous encouragement, support and for being there for me in the “dark moments” of my studies.

Finally, though a handful of names are mentioned here, a great number of people have contributed immensly in one way or the other towards the success of this thesis and my studies. May the good Lord bless all such individuals.

Tampere, January 2013

Nketiah Gabriel

TABLE OF CONTENTS

LIST OF SYMBOLS AND ABBREVIATIONS

ACC	Average correlation coefficient
AR	Autoregressive model
ASM	Angular second moment
BOLD - MRI	Blood oxygen level-dependent MRI
COM	Co-occurrence matrix
COST	European cooperation in science and technology
CT	Computed tomography
DICOM	Digital imaging and communications in medicine
DR	Computed radiography
DTI	Diffusion tensor imaging
F	Fisher coefficient
FID	Free induction decay
FLAIR	Fluid-attenuated inversion recovery
FLASH	First low angle shot
FSE	Fast spin echo
Gmax	Gluteus maximus
Gmed	Gluteus medius
GRE	Gradient echo
H-I	High-impact
H-M	High-magnitude
HU	Hounsfield units
IDM	Inverse difference moment
Iliop	Iliopsoas
IR	Inversion recovery
LDA	Linear discriminant analysis
L-I	Low-impact
M	Magnetization vector
MRF	Markov random fields
MRI	Magnetic resonance imaging
MRS	Magnetic resonance spectroscopy

M_{xy}	Transverse magnetization
M_z	Longitudinal magnetization
N-I	Non-impact
NMR	Nuclear magnetic resonance
ObtInt	Obturator internus
O-I	Odd-impact
PCA	Physiological cross-sectional Area
PCA	Principal component analysis
PD	Proton density
POE	Probability of error
REF	Reference
RF	Radio frequency
ROI	Region of interest
SE	Spin echo
SFR	Screen film radiography
SS	Sum of squares
STIR	Short-tau inversion recovery
T_2	Spin-spin relaxation time
T_{2*}	T_{2*} relaxation time
T_1	Spin-lattice relaxation time
TA	Texture analysis
TE	Echo time
T_I	Inversion time
TR	Repetition time
TSE	Turbo spin echo
VOI	Volume of interest
2D	Two-dimensional
3D	Three-dimensional

1. INTRODUCTION

Extraction of maximum information for clinical decision making is the prime aim of almost all medical imaging procedures [1; 2]. This goal has not been fully met, because, the images provided by medical devices are unable to give detailed diagnostic information in advance to help in clinical decision making. This is partly due to the fact that, details of tissues are very small compared to the resolution with which medical devices acquire images [2].

Though a considerable amount of success has been achieved in improving the resolution and contrast of medical images through the development of superior imaging techniques such as magnetic resonance imaging (MRI), the ability to extract detailed information from medical images usually depends on manual visual assessment capabilities and experience of radiologists. This usually limits the amount of information that can be obtained from medical images, because, visual assessment is subjective and the human eye-brain interface can only appreciate limited level of complexity. [1; 2.] The situation even becomes more complicated in cases where certain microscopic changes that occur within tissues cannot appear on medical images for visual assessment.

Quantitative or automated method of analyzing medical images known as texture analysis (TA) therefore serves as an important tool for extracting optimal information from medical images as it is highly sensitive in detecting subtle and microscopic changes in images. TA is known to be very specific, reproducible, objective and accurate in describing alterations in tissues; for instance, the use of MRI TA in characterizing normal and pathological muscles tissues [3; 4; 5] has proven to be more efficient than manual means. As a result, texture analysis for diagnostic applications has attracted much attention in the field of research.

Skeletal muscles are known to adapt to different forces resulting from load-associated differences by changing in structure [6; 7]. However, it is not known how texture in different muscles differ from each other, especially with respect to different athlete groups as the type of training and loading differ from athlete to athlete. There have been some successful studies on the use of MRI TA in analyzing structural changes in muscles due to training [8]. However, these analyses were performed in two-dimensional (2D) environment which is a representation of a single two-dimensional slice of a three-dimensional (3D) structure over an image volume. Hence there is the possibility that the 2D methods could not point out certain minute details that might still be of clinical importance. The objective of this thesis is to:

1. determine whether textural differences exist in hip muscles due to exercise-loading differences

2. compare the effectiveness of 3D and 2D texture analyses in detecting and charactering these loading differences.

2. MEDICAL BACKGROUND

2.1. Anatomy of muscle

A muscle is a specialized group of fibrous tissues in the body that has four major functional or characteristic properties, namely: contractility, excitability, extensibility and elasticity [9]. Muscles are mainly responsible for body movements and maintaining posture of the body. There are three types of muscles in the body: smooth, cardiac and skeletal muscles.

Smooth muscles make up the walls of hollow organs and tubes in the body such as blood vessels, the digestive and urogenital organs. They help advance and control flow. Smooth muscles are characterized by elongated cells with tapered ends, no striations and a centrally located single nucleus. They are unconsciously controlled by the body. Cardiac muscles comprise most of the heart. The muscle cells are striated and have one centrally located nucleus. Cardiac muscles are autorhythmic and are involuntarily controlled by the autonomic nervous system and the endocrine system. [9; 10.]

Skeletal muscles are composed of bundles of muscle fibers called fascicles. Each skeletal muscle fiber consists of a long, striated, cylindrical and multinucleated cell surrounded by a connective tissue called endomysium. Each bundle or fascicle is enclosed in a fibroadipose tissue called perimysium while the entire muscle is ensheathed by a fibrous connective tissue known as epimysium. [8; 9; 10; 11.] Figure 2.1 below shows the structural arrangement of a skeletal muscle.

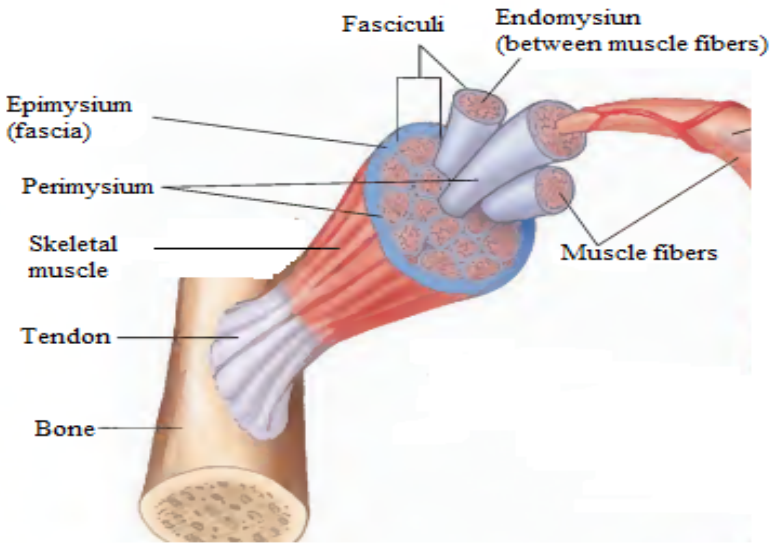

Figure 2. 1. *Structure of a skeletal muscle [10]*

Skeletal muscles constitute about 40% of the body weight. Unlike smooth and cardiac muscles, skeletal muscles are consciously controlled (voluntary muscles) and are mainly responsible for locomotion, facial expression, posture and respiratory movements. [8; 9; 10; 11.]

Muscles attached to the hip are mainly made up of skeletal muscles and hence responsible for the movement of the leg. These muscles are categorized according to their position of insertion to the hip. For instance muscles attached to the trochanter of the femur can be grouped into superior (example: obturator internus), posterior (gluteus maximus, gluteus medius), inferior and anterior (iliopsoas) muscles. These groups perform specific functions by acting as rotators, extensors, abductors and flexors of the femur. [10; 12.]

2.2. Effects of exercise on muscles

The amount of force produced by a muscle depends on the muscle fiber cross-sectional area, number of muscles fibers and the muscles fiber type [8]. During training or exercise, muscles adapt to the forces or loads that they are subjected to, depending on the type of exercise or training. The adaptation leads to changes in the size, strength, architecture and mass of the muscles involved. [6; 7; 9.]

As one exercises, the physiological cross-sectional area (PCA) of the muscles actively involved in the exercise increases and so does the muscular strength. The increment is due to the fact that the cross-sectional area of the individual muscle fibers increases (hypertrophy) in response to exercise. Hypertrophy continues throughout the training or exercise until the muscles strength adjust to the forces or loads they are subjected to [8; 9]. Conversely, muscle mass and thickness decrease with less frequent usage of muscles. [13; 14; 15.]

2.3. Muscle imaging

A variety of modalities exist for imaging skeletal muscles. The commonly known modalities include radiography, computed tomography (CT), ultrasound and magnetic resonance imaging (MRI). A comparison of these modalities with respect to skeletal muscle imaging is given in Table 2.1. Other techniques such as diffusion tensor imaging (DTI) and magnetic resonance spectroscopy (MRS) are under research.

Table 2.1. *Comparison among common muscle imaging modalities*

Imaging modality	Advantages	Disadvantages
Radiography	Fast imaging time Readily availability User friendly and familiarity with medical professionals	Superimposition of structures Blurring Poor contrast resolution Radiation dose required
CT	Good contrast resolution	Radiation dose required
Ultrasound	Less costly No radiation dose required Average spatial resolution Real-time display capabilities	Operator dependent
MRI	Excellent contrast Availability of different imaging techniques No radiation dose required	Very expensive Cumbersome

2.3.1. Radiography

Radiography is one the oldest imaging modalities in medical history. It is still widely used and serves as the first point of call for the diagnosis of many clinical conditions. This is because of its wide availability, fast imaging time, low cost, non-invasiveness, user friendliness and most importantly its familiarity with medical professionals [16]. In conventional radiographic imaging, X-rays are produced by bombarding a metal target with high energy electrons. The emitted uniform beam of radiation is transmitted through the body where it is absorbed and modified as it interacts with tissues. The resultant beam that penetrates the target is recorded on a film and further processed into images.

The short comings of the conventional radiography or screen film radiography (SFR) such as long term storage difficulties, use of hazardous film materials, fixed non-linear scale response and dose problems led to the development of digital or computed radiography (DR). In computed radiography, a photostimulable phosphor plate is used for detection of X-rays instead of conventional film screen. This is later converted into digital format through the use of photomultiplier tube and other electronic processes. DR offers numerous advantages over SFR such as improved detector efficiency, linear detector response, dose reduction, digital processing capabilities for image storage, retrieval, display and transmission. [17; 18; 19.]

With development of newer technologies such as MRI and ultrasound, the use of radiography in muscle imaging or studies is diminishing due to its poor contrast resolution. In radiography, image contrast depends mainly on the relative differences in X-ray attenuation between different tissues. However, the density differences between various soft tissues in skeletal muscles (tendons, fat, ligaments, and fascial structures) are

small. Hence, radiographic images of skeletal muscles have poor contrast. This makes the direct visualization and subsequent characterization of muscles from their surrounding soft tissues difficult. Besides this, radiographic imaging also suffers from superimposition of structures and blurring. [20; 16.]

2.3.2. Computed tomography

Computed tomography is an imaging modality that produces cross-sectional images as well as 3D images from acquired projection images of a target area using X-ray or ionizing radiation. The projection images are acquired through X-ray scans, during which single exposures are made at certain degree or angle intervals. During the process, the X-ray source and the detector rotate synchronously around the subject and take sequential scans at fixed angular intervals. X-ray photons are transmitted through the target area along a single projection line and the radiation attenuation properties for that part of the body are measured as Hounsfield units (HU). [21; 22.] The attenuation profiles or properties at different angles are then filtered and reconstructed to produce cross-sectional images [20]. A cross-section or slice is produced when the assembly makes 360 degrees rotation around the subject to acquire sequential planar projection images of the selected field.

Unlike radiography, CT offers a better contrast resolution, does not suffer from superimposition and can clearly distinguish various tissues within and around muscles. Also, the recent development of spiral scanning techniques and multi-detector row CTs has tremendously increased data acquisition and reconstruction capabilities of CT imaging. This has enabled direct visualization of skeletal muscle from almost any direction without loss of resolution, and has also decreased scanning times. [20.]

2.3.3. Ultrasound imaging

The use of ultrasound for medical applications has increased progressively since it was first discovered. It is by far known to be most widely used, cheapest and convenient diagnostic modality in medicine. Its usage spans across all fields in medicine from diagnosis to treatment. This is because it is non-ionizing, non-invasive and has real-time display capabilities. [11; 23; 24.]

Ultrasonography involves the use of sound waves at frequency range of 1-10MHz, beyond human hearing range. Sound waves within this range are generated and transmitted to the imaging target by a transducer probe. The intensity of reflected waves and delay time between the transmission of the sound waves and the arrival of the reflected acoustic pulses at the probe are measured. These are further processed to give the relative location and image of the object. These two parameters depend on the acoustic impedance of imaging tissues. When an ultrasound beam travels between tissues with different acoustic impedances such as from muscle to bone, a part of it is reflected at the interface of the two tissues. Since acoustic impedance differs among different tissues

such as fat, muscle, fascia, blood and bone, images of different tissues can be obtained and distinguished. The use of Doppler imaging and different scan modes can help give more detailed information. [9; 11; 23.]

Beside the reasons stipulated above, the use of ultrasound in muscle imaging still receives much attention in research because of its multi-planar evaluation, excellent spatial resolution, better clinical correlation and its ability to fairly distinguish normal muscles from surrounding structures and muscular abnormalities [23; 24]. The major disadvantage of ultrasonography is that, it is operator dependent [9; 11].

2.3.4. Magnetic Resonance Imaging

The development of MRI technique is one of the most important, promising and radical technological changes in field of medical imaging in recent times. Besides its non-invasiveness and radiation free advantages, it offers three-dimensional (3D) tomographic view of internal physiochemical and biochemical processes of soft tissues with more excellent contrast than other imaging modalities. The availability of different MRI techniques such as diffusion and perfusion measurements, *in vivo* spectroscopy, fiber tracking, relaxometry, functional MRI and BOLD MRI also help in giving detail diagnostic information [25]. The principles of MRI are described in detail below, as it is the imaging modality used in this thesis.

MRI is principally based on the measurement of externally emitted radio frequency waveforms known as nuclear magnetic resonance (NMR) signals. A nucleus is said to be MR active if it has an odd mass number such that the spins of its protons and neutrons do not cancel each other out, resulting in a net spin. Under normal circumstances, each MR active nucleus rotates or spins on its axis and at same time their magnetic moments are randomly oriented. [25; 26; 27.]

MR signal generation

When a nucleus (subject) is placed into stronger external magnetic field (β_0), the influence of β_0 causes spinning hydrogen protons in the subject to precess or wobble around the β_0 axis. The frequency or rate of precession is governed by the Larmor equation

$$\omega_0 = \beta_0 * \gamma \qquad (1)$$

Where, ω_0 is the precessional frequency of the protons and γ is the gyromagnetic ratio. Hydrogen nucleus (^{1}H) is mostly used in medical MR imaging due to it abundance in the human body and its ability to produce large magnetic moments [26; 27].

The application of β_0 also causes the magnet moments of the protons to align themselves either in parallel or opposite (anti-parallel) to the direction of β_0. This results in a net magnetization vector M, in the direction of β_0, which is the cumulative effect of all the magnetic moments of the nuclei. When an external radio frequency (RF) pulse

with the same frequency as that of the precession protons (ω_0) and at 90 degrees to β_0 is applied to the precessing protons, the protons absorb energy from the RF pulse and precess in phase. This causes the net magnetization vector M to tilt by a certain angle θ into the x-y plane thereby producing two magnetization components: longitudinal (M_z) and transverse magnetization (M_{xy}). If a RF pulse with proper amplitude and duration is applied, a situation is created whereby the number of protons that are aligned parallel and anti-parallel to the direction of β_0 become equal. At this point, the longitudinal magnetization (M_z) component tilts through 90° to create a net magnetization vector precessing in the transverse plane without any M_z. This is known as RF tilting. As this transverse magnetization vector precesses, it passes across and induces a current in a receiver coil located in the transverse plane. This recorded current is referred to as MR signal. [26; 27.]

Relaxation times

When the RF pulse is switched off, the induced signal or current in the receiver coil gradually dies off because the net magnetization vector in transverse plane decreases as precessing protons begin to dephase. This is known as free induction decay (FID). Turning off the RF signal leads to two most important processes: T_1 recovery, T_2 decay. First, the protons emit their absorbed energy causing the net magnetization vector to recover and realign in the direction of β_0. T_1 recovery indicates or depends on how quickly the protons can emit or exchange their absorbed energy with neighboring tissues or protons, hence the term spin-lattice for T_1.

Secondly, the precessing protons become dephased and the net magnetization vector in transverse plane decays because, each proton experiences an external self-generated magnetic field of its neighbouring protons. This is termed T_2 decay or spin-spin relaxation. In addition, an exponential rate of decay in the transverse magnetization known as T_2* occurs due the inhomogeneities in the external magnetic field. [26; 27.]

Contrast mechanisms

Besides proton density (PD), T_1 and T_2 also provide contrast in MR images. This is because, different tissues in the body have different T_1 and T_2 times due to differences in their chemical composition and physical states [26; 27; 28]. For instance fat is known to have a shorter T_1 and T_2 times than water. Also, pathological tissues are generally known to have longer T_1 and T_2 values than normal tissues. Tissues with long T_1 time appear dark on a T_1 weighted image whereas tissues with long T_2 values appear bright on a T_2 weighted image. [28.]

Repetition time (TR) and echo (TE) time are extrinsic contrast parameters (system operator controlled) that can also be adjusted to control T_1 and T_2 times to obtain contrast between tissues. TR is the time difference between applications of successive RF pulses. It affects T_1 contrast. On the other hand, TE is the time between the application of the RF pulse and the detection of MR signal and it affects T_2 contrast. By adjusting TE and TR,

a particular type of contrast can be emphasized while the other parameters are suppressed. This is achieved through T_1, T_2 weighting and proton density (PD) weighting imaging. [26; 27; 29.]

During T_1 weighting imaging, TR is selected to be very short such that only tissues that are able to recover most of their longitudinal magnetization during that TR give high MR signal. These tissues therefore appear as white whereas tissues with long TR appear as black. With T_2 weighting however, long TE is selected such that tissues with long T_2 decay time give high MR signal and therefore appear as bright or white. Tissues with long T_2 time are capable of retaining most of their transverse coherence during TE period.

Proton density weighed imaging on the other hand achieves contrast by emphasizing on number of hydrogen protons. This is done by nullifying both T_1 and T_2 effects through the use of long TR and short TE respectively. Tissues with high proton density give high MR signal and therefore appear as white, whereas those with less PD appear as black. [26; 27; 29.]

MR signal localization

In order to know the tissue from which the MR signal is coming, three special types of orthogonal magnetic coils known as X, Y and Z gradients are used. The application of these gradient magnetic fields changes the magnetic field strength along the X, Y and Z axes respectively, and also alters the precessional frequency and the precessional phase of hydrogen protons in the imaged region. This is used in spatial encoding – identification of the three-dimensional spatial position of the MR signal. [26; 27; 29.]

Spatial encoding involves three processes or functions: slice selection, frequency encoding and phase encoding, each of which is specifically performed by one of the three gradients depending on the selected scanning plane. The raw data contained in the signal from the scanned field of view constitutes the frequency and phase of the signal. This is mapped and stored in a matrix known as k-space which is further processed into an image by means of Fourier transform. [26; 27; 29.]

MR pulse sequences

MRI pulse sequence is a series of combined RF pulses and gradient wave forms that are applied at intervening time periods during MR image acquisition process to obtain different images of different anatomical structures and pathologies in the body. They are used to rephase spins and to remove inhomogeneity effects in order to obtain sufficient signal to produce an image. They are also used to manipulate TE and TR to produce different types of image contrasts. [26; 27.] There are a variety of pulse sequences that are used in medical MR imaging, however, the most important and commonly used ones are the spin echo (SE) sequence, the inversion recovery (IR) sequence and the gradient echo (GRE) sequence. [29]

In spin echo (SE) sequence, the application of a slice-selective 90° RF pulse for excitation is followed by a 180° RF pulse, which is delivered after half of the echo time (TE) has elapsed, to rephase the spins and to regenerate signal in the receiver coil. SE sequences have a major advantage of providing good quality images and serve as the standard sequence for producing T_1, T_2 and PD weighted images of any part of the body. Conversional SE sequences have long acquisition time which makes it very sensitive to motion artifacts. This problem is however solved by employing the use of fast or turbo spin echo sequences (FSE/TSE) which make use of a train of 180° RF pulses to rephase the spins. [29.]

During inversion recovery sequence, an initial 180° inverting pulse is first applied to flip the net magnetization vector M through 180° into a negative direction anti-parallel to β_0. This is followed by applying a 90° RF excitation pulse within a time interval TI (inversion time) after the 180° inverting pulse has been turned off and M has gone through some relaxation towards β_0 direction. A final 180° RF pulse is then applied to rephase the spins thereby producing echo signals for image construction. Contrast in this imaging sequence therefore depends on TI. Short TI inversion recovery (STIR) sequence and the fluid-attenuated inversion recovery (FLAIR) sequence are the most clinically important IR sequence techniques widely used in imaging. STIR uses short TI and it is widely used in fat suppression whereas FLAIR uses long TI. IR sequences are mostly used in T_1 weighted or fat-suppressed imaging. [26; 29.]

Gradient echo sequence involves the use of gradients to produce echo signal instead of RF pulses. During this sequence, a radio frequency pulse with a tilting angle usually less than 90° is first applied to partly flip the precessing net magnetization vector into the transverse plane. A negative frequency encoding gradient is then applied to dephase the precessing spins. The polarity of this gradient is subsequently reversed (positive) to rephase the spins. This leads to production of a signal called gradient echo in the receiver coils. GRE sequences have shorter repetition and imaging time than SE and IR sequences. Hence, GRE sequences are less prone to motion artifacts and are preferred in image acquisitions where short scan time is of key importance. [29; 30.] On the other hand, GRE sequence images are more sensitive to external magnetic susceptibility because of the rephasing gradient's inability to completely rephase or eliminate the T_2* dephasing effects produced by inhomogeneities [26].

MR imaging of skeletal muscles

MRI is considered as the most suitable imaging modality for evaluating muscle anatomy, morphology and physiology because of its superior soft tissue contrast and spatial resolution. It is extremely sensitive in detecting subtle muscle lesions that result from pathological conditions such as atrophy, fat infiltration and edema, as well as detecting degree of active involvement of a muscle. It is also capable of ascertaining the necessity for the muscle biopsy and subsequently guiding the biopsy so as to give accurate diagnoses. [2; 3; 11; 20; 31; 32.]

In ideal situations, the signal intensity of a skeletal muscle is usually higher than that of water on a T_1 weighted image but much lower than that of fat and water on a T_2 weighted image. On inversion-recovery and fat-suppressed T_2 weighted images however, normal muscle has a much lower signal intensity than that of water but higher than that of fat. Also the permysium appears as hyperintense on T_1 weighted images due its fatty nature while the epimysium is hypointense on both T_1 and T_2 weighted images due to its fibrous composition [11]. The remaining parts appear striated and "feathery". Pathological conditions in muscles may therefore shorten T_1 time due to fatty infiltration or prolong T_2 time due to muscle edema. For this reason, most skeletal muscle MR imaging protocols for diagnostic purposes usually include a T_1 weighted sequence and one fluid-sensitive sequence such as STIR or fat-suppressed T_2 weighted sequences. [11; 20; 31; 32.] Figures 3 and 4 below illustrate ultrasound images of a healthy and diseased skeletal respectively.

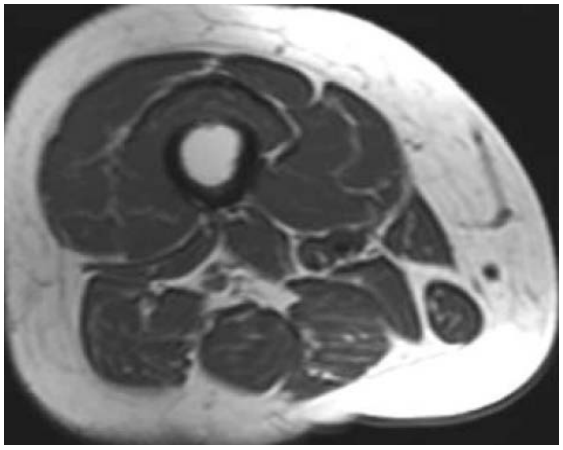

Figure 3: *Axial T1-weighted image of the thigh demonstrating the normal appearance of skeletal muscle [31]*

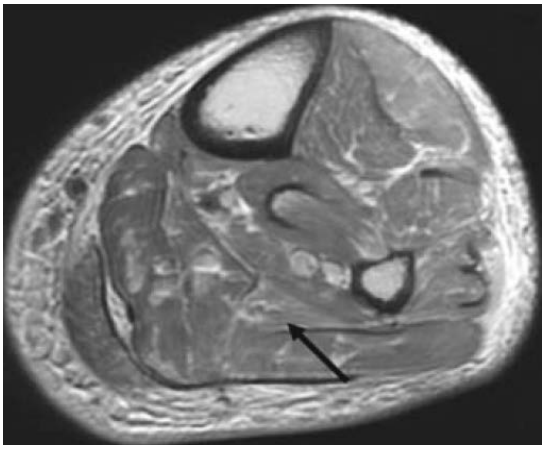

Figure 4: *Axial proton density-weighted image of the shank showing mild loss of muscle bulk and fatty infiltration (arrow) [31]*

T_1 weighted images are for detection of fat related abnormities whereas fat-suppressed T_2 weighted and STIR images are very effective in detecting fluid related abnormalities such as edema. Spin-echo sequences are most commonly used, though GRE sequences are sometimes used in some unique situations. Contrast agents are not usually used in most muscle MR imaging [2; 3; 11; 20; 31; 33].

3. TEXTURE ANALYSIS

Even though texture is a common inherent feature of all object surfaces which is easily perceived by humans, there is no precise definition for it. It describes visual patterns and surface characteristics of objects such as color, size, shape, brightness, uniformity, smoothness, granulation, as depicted below (Figure 3.1). Image texture can be defined as similarity groupings, appearance, structure or arrangement of objects within an image as a result of spatial variations in pixel intensity (grey value) distributions in the image. [21; 25; 34; 35.]

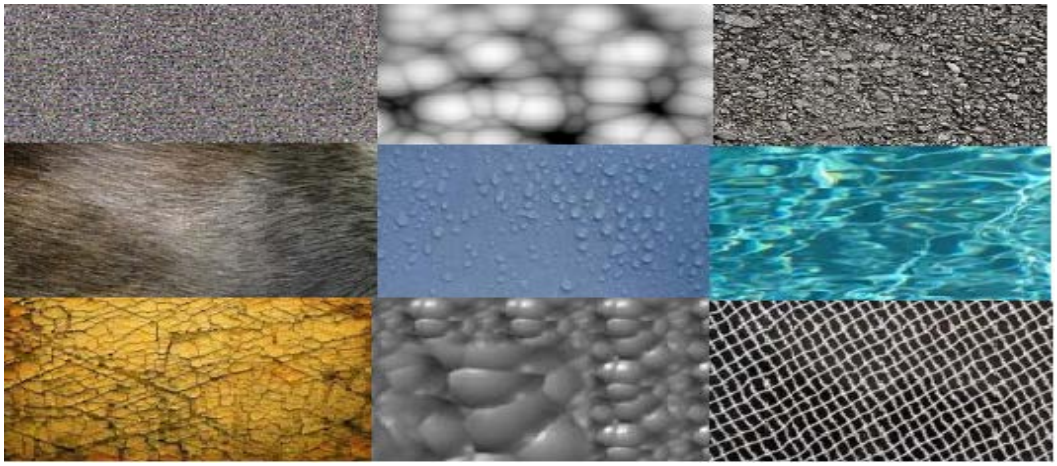

Figure 3.1. *Example of different image textures*

Image texture is known to be a valuable source of visual information for medical purposes, but humans unlike computers possess limited sensitivity to textural features [1; 2; 36]. Also, each of the muscle imaging modalities described above has limitations such that they do not offer the best quality images for visual assessment, therefore, some slight but clinically important changes that occur in tissues may not be visible on images. This implies that visual assessment alone cannot reveal all the necessary detail information contained in an image.

Automatic or quantitative texture analysis (TA) offers a better way of extracting more detail information from images because of its computational advantage, high sensitivity, specificity, and the availability of numerous TA methods. Hence, TA for medical applications has recently gained much attention in research. Texture analysis is a series of mathematical techniques used in quantification and evaluation of spatial variations in pixel intensities within a digital image. It enables the use of mathematical parameters (textural features) computed from pixel distributions, in characterizing texture types in an image. [1; 2; 25; 34.] Texture analysis was originally developed for processing of satellite images and aerial photographs, geological survey, and remote sensing [1; 2; 5].

However, its numerous advantages have seen its application across several areas, spanning from quality control to security.

The application of TA methods for analyzing medical images took off in the late 1970s when image digitization began. This has advanced tremendously lately to involve diagnosing diseases, following healing progress, distinguishing between pathological and normal tissues. [2; 28.] Several studies have found TA to be useful in obtaining detailed, accurate and reliable diagnostic information from medical images to assist in clinical decision making. This technique has been investigated to have the ability to measure changes in trabecular structure thereby making it useful in early detection of periprosthetic osteolysis [37]. TA has also been shown to be capable of distinguishing between normal and abnormal lung tissues in chest radiography scans [38; 39; 40]. Texture analysis of CT images has also been proven to be useful in early detection of ischemic stroke and quantification of the extent of affected areas, and classifying obstructive lung diseases and normal lung tissues [36; 41].

Texture analysis of muscle ultrasound images was successfully applied in early diagnosis of different muscle abnormalities [24; 42; 43], classification of pathological tissues [44] and verification of quality of beef [45]. Additionally, Herlidou et al [4] compared automated and visual texture analysis of MRI images in characterization of normal and diseased skeletal muscles, and concluded that texture analysis gives more accurate discrimination between control and pathological tissues than visual analysis. TA of MR images has been successfully used in early diagnosis of diseases [46; 47] and monitoring effect of therapy during follow ups [48].

3.1. Steps in quantitative texture analysis

Quantitative texture analysis involves three major steps: feature extraction, feature reduction and selection, and texture classification.

3.1.1. Feature extraction

In image texture analysis, feature extraction is the process of computing texture features of a defined region in an image to quantitatively describe its texture. It involves computation of characteristic numerical parameters that describe textural properties of an image. It is the basis of image texture analysis upon which further steps and processes depend. The computation of numerical parameters is done on a predefined homogeneous tissue region by moving a small rectangular window across the image and then computing the corresponding texture parameter at each position. In most medical applications, the small homogeneous tissue region is selected manually and it is often referred to as region of interest (ROI). [25.]

Texture parameters can then be used to produce feature maps. A feature map is an illustration of a selected texture parameter’s intensity across the image. Therefore, by assigning a parameter to a particular texture property, the corresponding feature map can

indicate places in the image where this property is dominant (white) and regions where it is less or absent (dark). Examples of texture parameters that can be computed are variance, skewness and mean. [25.] There are several methods that can be used in texture feature extraction. These methods are explained in detail under section 3.2 below (approaches to texture analysis).

3.1.2. Feature selection and reduction

In order to reduce complexity and irrelevancy, as well as improve accuracy and speed of image texture classification process, the huge amount of data obtained from the feature extraction process is subjected to feature selection and feature reduction techniques. These provide best data for classification and reduce the dimensions of feature vectors respectively [25; 28].

Methods involving the use of Fisher coefficient (F) and lowest probability of error & average correlation coefficient (POE+ACC) are usually used in feature selection whereas principal component analysis (PCA) and linear discriminant analysis (LDA) are the most commonly used methods in feature reduction [25; 28].

3.1.3. Texture classification

Classification is a process of assigning a physical object or event to one of a set of predefined categories [49]. The main objective of texture classification is to assign an unknown sample image to one of a set of known texture classes. During the process, a classifier is trained to determine which of a finite number of physically defined classes (such as normal and abnormal tissue) a textured region belongs to, by comparing textural features of test image to that of a training set with known category and then assigning the textural feature of test image to the category that it matches most. [49.]

Texture classification can be supervised or unsupervised. In a supervised classification, prior knowledge about the textures to be classified is made available by some other independent means. For instance, a biopsy can first be used to determine whether a tissue is normal or diseased before the texture classification process. Supervised classification can be parametric in which certain assumptions about the distribution of features are made or non-parametric where no assumptions are made about the forms of feature distribution. Unsupervised classification is however automatic without prior knowledge. [50.]

3.2. Texture analysis approaches

As stated earlier, a wide range of different approaches or methods exist that can be employed in texture description or computing texture parameters. It is practically impossible to tell beforehand which method will be most suitable for describing texture properties for a given application, however, optimal results can be obtained by combing some of the methods. These approaches are generally grouped into four categories:

structural-based, statistical-based, model-based and transform-based approaches. [25; 28; 34; 36.]

3.2.1. Structural approaches

Structural approaches to texture analysis or description involve the use of well-defined primitives in representing texture. With this method, an object is basically represented by primitives that form its borders, hence mathematical morphology operators serve as powerful tools for structural texture analysis. Key to texture description in this approach is the description of primitives and the rules of placement. Structural approaches give a good symbolic description of an image, however, they are most suitable for image synthesis rather than analysis. [25; 34; 51.]

3.2.2. Statistical approaches

Statistical approaches use the spatial distribution of grey level values and relationships between pixels within an image in describing texture. These approaches are widely used in medical image analysis. They are best suited for this purpose because tissues usually have random, non-homogeneous structures. They are also suitable for analysis of images with irregular distributions of pixel intensities. [3; 4; 36.] The statistical parameters or features used in texture description are statistical measures derived from 5 different statistical image descriptors, namely: histogram, gradient, autocorrelation function, run-length matrix and co-occurrence matrix. Statistical parameters can be grouped into fist-order, second-order and high-order statistics depending on the number of pixels that define a local feature. [28.]

Fist-order and second-order statistical parameters are most commonly used in TA. First-order statistical parameters describe image properties or local features that depend only on the individual pixel values. They are mostly derived from image histogram. On the other hand, second-order statistical parameters describe properties of grey level pairs. These parameters are derived from co-occurrence matrix and gradient matrix. They are known to be capable of achieving higher discrimination indexes than transform and structural methods. Statistical features derived from the co-occurrence matrix are the most widely used in texture analysis. Parameters from run-length matrix are usually considered as high-order statistics. [36; 51; 52; 53; 54.]

3.2.3. Model-based methods

Model-based methods of texture analysis involve construction of a parametric generative image model of the observed intensity distribution and using the corresponding estimated model parameters as textural feature descriptors [49]. Models commonly used in deriving textural features are Markov random fields (MRF), autoregressive model (AR) and fractals. Markov random fields are capable of capturing the local (spatial) contextual

information contained in an image based on the assumption that the intensity at each pixel in the image depends solely on the intensities of the neighboring pixels. [55.]

Fractals are set of self-similar functions that are characterized by fractal dimension. Fractal dimension is the measure of perceived roughness of a surface. It therefore serves as the texture parameter (feature) for image texture analysis. A larger fractal dimension implies a rougher texture and vice versa. [55; 56.] Autoregressive model uses the description of shapes within an image in analyzing or describing texture by finding relations between groups of neighboring pixels. The main disadvantage of model-based methods is the computational complexity involved in estimating these model parameters. [34.]

3.2.4. Transform methods

In transform methods, texture parameters are derived from the analysis of frequency and scale contents contained in an image. Fourier, Gabor and wavelet transforms are usually used. Fourier transform describes the global frequency content of an image without any reference to localization in the spatial domain which results in poor performance. [49.]

Gabor transforms are frequency and orientation specific. As a result of this, their practical applicability is limited because it is usually impossible to obtain single filter resolution at which a spatial structure in natural textures can be localized. However, they offer a means of achieving better spatial resolution. With wavelets, the frequency content of an image can be analyzed within different scales of that image. The possibility of varying the spatial resolution and the availability of wide range of wavelet function choices make wavelet transforms most suitable for texture analysis in specific applications. [25; 34; 49; 55.]

3.3. Texture parameters

There are a wide variety of parameters that can be used in texture description or analysis. However, the parameters discussed in this section are the most commonly used in many texture analysis studies for medical applications. Also, these are the main texture parameters calculated by the texture analysis application software – MaZda (4.6) used in this thesis. MaZda is a computer program for calculation of texture parameters (features) in digitized images. It was developed at the Institute of Electronics, Technical University of Lodz (TUL), Poland, under a project instituted by the European Cooperation in Science and Technology (COST): “Quantitation of Magnetic Resonance Image Texture” (COST Action B11). [25.] Table 3.1 below gives the summary of these texture parameters. The mathematical notations for these parameters can found in [25].

Table 3.1. *Texture parameters computed by MaZda 4.6 [57].*

Image descriptor method	Texture parameters derived from descriptor	Texture analysis approach
Histogram	Mean	Statistical
	Variance	
	skewness	
	kurtosis	
	1-% percentile	
	10-% percentile	
	50-% percentile	
	90-% percentile	
	99-% percentile	
Absolute gradient	Mean absolute gradient	Statistical
	Variance of absolute gradient	
	Skewness of absolute gradient	
	Kurtosis of absolute gradient	
	Percentage of pixels with nonzero gradient	
Co-occurrence matrix	Angular second moment contrast	Statistical
	Correlation	
	Sum of squares	
	Inverse difference moment	
	Sum average	
	Sum variance	
	Sum entropy	
	Entropy	
	Difference variance	
	Difference entropy	
Run-length matrix	Short run emphasis moments	Statistical
	Long run emphasis moments	
	Grey level nonuniformity	
	Run length nonuniformity	
	Fraction of image in runs	
Wavelet	Energy of wavelet coefficients in sub-bands at successive scales; Maximum 4 scales each with 4 parameters	Transform
Autoregressive model	Vectors of model parameters ($Theta$: $\theta_1, \theta_2, \theta_3, \theta_4$)	Model-based
	Standard deviation of the driving noise, σ	

These texture parameters are derived from the commonly used image texture descriptor methods. The methods and the corresponding texture parameters that can be derived from them are explained in detail below.

3.3.1. Histogram

Digital images are composed of minute rectangular blocks or elements called pixels, or minute cubic blocks called voxels, each of which is represented by a set of coordinates in space. Each pixel or voxel possesses a certain value that indicates the grey level intensity of that pixel. The count of how many pixels possess a specific grey level value is plotted as a histogram representing each grey level value against the number pixels that possess that value. Statistical measures or texture parameters that are derived from image histogram for texture analysis include mean, variance, kurtosis, skewness and percentiles. [34; 58.]

Mean depicts the average grey level intensity of an image. Variance is a measure of the extent to which the grey level values are distributed away from their mean; which is an indication of image roughness. Skewness describes the histogram symmetry about the mean; positive skewness is indication that an image has high grey level values such that majority of them lie above the mean, and vice versa. Kurtosis is a measure of peakness or flatness of a histogram. It indicates uniformity of the grey level distribution relative to a normal distribution. A histogram with high or positive kurtosis has sharp or distinct peak near the mean while that of a negative or low kurtosis is flat or round near the mean. Percentiles are used in estimating the highest grey level value under which a given percentage of the pixels in the image fall. [34; 58.]

3.3.2. Absolute gradient

The measure of spatial variation in grey level intensities across an image is referred to as the gradient of that image. An image is said to have high gradient value if the grey level changes abruptly between white and black. Conversely, the gradient is said to be low if the variation is gradual. [5; 34; 58.]

Texture parameters that can be derived from absolute gradient are mean of absolute gradient, variance of absolute gradient, kurtosis of absolute gradient and skewness of absolute gradient. Mean of absolute gradient measures the mean grey level variation across the image and variance of absolute gradient measures how the variations are from the mean. The rest describe the absolute gradient as in the case of histogram explained above. [5; 34; 58.]

3.3.3. Co-occurrence matrix

Co-occurrence matrix (COM) is an estimation of the joint probability ($P_{\partial\theta}(i,j)$) of two pixels, separated by distance d pixels apart ($d = 1, 2, \dots, 5$) along a defined direction θ ($0°, 45°, 90° \; and \; 135°$) having co-occurring grey level values i and j [25]. The joint probability is computed for each ROI using different combinations of d and θ to give a square matrix called COM. Thus COM is the count of pairs of pixels that possess equal or specific grey level values in a certain direction and at a specific distance apart. Texture parameters computed from COM are angular second moment (ASM), contrast,

correlation, sum of squares (SS), inverse difference moment (IDM), sum average, sum variance, sum entropy, entropy, difference variance and difference entropy.[35; 36; 57; 58; 59.]

Angular second moment (ASM) is a measure of uniformity or homogeneity of an image. A high ASM value is recorded when there are high differences in the COM entries, whereas it is low when all the entries of the COM are equal. A high ASM value is an indication of greater homogeneity and more regularity in image texture. Contrast is the relative variation between grey level values of different objects in the image. Correlation is a measure of grey level linear-dependencies in the image. Sum of squares computes variance in the COM. [35; 36; 58; 59.]

Inverse difference moments also measures homogeneity just as ASM. Sum average is the average of normalized grey level image in the spatial domain while sum variance indicates how much the distribution of sum probability differs from its mean. Sum entropy and difference entropy measure the randomness of grey level distribution; thus they measure disorder in an image, while entropy is an indication of the complexity within an image. The highest entropy is obtained when all the probabilities are equal. High entropy value(s) indicates the grey level distribution is highly indiscriminate, leading to more complexity or disorder in the image. [28; 34; 35; 36; 58; 59.]

3.3.4. Run-length matrix

A grey level run is the maximal sequence of consecutive pixels with the same grey level value or intensity [34]. It is characterized by length and direction of the run. The run-length matrix therefore computes the number of runs for a defined grey level value and length in a certain direction $\theta°$. It gives information about the number of collinearly connected pixels having the same intensity level in a defined direction. [51.] Four directions; $0°, 45°, 90°$ and $135°$ are used in the matrices calculations. Texture parameters extracted from the run-length matrix are short run emphasis inverse moments, long run emphasis moments, grey level nonuniformity, run length nonuniformity and fraction of image in runs. [5; 34; 57; 58.]

Short run emphasis inverse moments and long run emphasis moments are measures of proportions of runs in the image that have short length and long lengths respectively. Images with short runs have fine texture while coarse textures are known to have relatively long grey level runs. Grey level nonuniformity is a measure of uniformity in run distribution among the grey levels. Uniformly distributed runs have small grey level nonuniformity values and vice versa. Run length nonuniformity on the other hand is an indication of how uniformly grey levels are distributed among the runs. Fraction of runs in image compute the percentage of image pixels that are part of any of the runs defined for computing the matrix. [5; 34; 57; 58.]

3.3.5. Wavelets

The use of wavelets in describing texture involves analyzing the frequency content of an image within different scales of that image [34]. Wavelets provide a means of separating image signal into different frequency components, and then studying each component with resolution matched to its scale [57]. This is achieved by performing wavelet decomposition of the image signal using high and low pass filters or Haar function. The output gives a set of wavelet coefficients corresponding to different scales and to different frequency directions. [28; 57.]

Energy of wavelet coefficient – the measure of frequency content of an image on a given scale and in a given direction is an example of a wavelet derived texture parameter. The wavelets techniques have gain attention in recent times because they are capable of localizing signal spectral features in time (space). [34; 57.]

3.3.6. Auto-regressive model

Texture description based on the auto-regressive model is based on the fact that each pixel in an image is linearly dependent on it neighbors [60]. Hence, a pixel's grey level value is a weighted sum of the grey level values of its neighboring pixels. The grey level value of particular a pixel can therefore be estimated from the grey level values in its defined neighborhood. It uses linear estimates of a pixel's grey level in characterizing texture. [34; 51; 60; 61.]

The characteristics of an image texture may be determined by manipulating the estimated value against its real value. Five parameters are usually computed for each selected ROI, consisting of coefficients of four neighboring pixels ($Theta: \theta_1, \theta_2, \theta_3, \theta_4$) and standard error of noise ($sigma, \sigma$). The computed coefficients are similar in images with coarse texture whereas there are wide variations in the coefficients of fine textures. [51; 60; 61.]

4. MATERIALS AND METHODS

4.1. Study subjects

A total of 111 adult female volunteers consisting of 91 highly active athletes and 20 non-athletes were used in this study. They were obtained from a previous study carried out by the UKK Institute for Health Promotion Research, Tampere, Finland. The athletes comprised 9 triple-jumpers, 10 high-jumpers, 10 soccer players, 9 squash players, 17 power-lifters, 18 endurance runners and 18 swimmers. The non-athlete subjects (n = 20) were clinically healthy students recruited from Pirkanmaa University of Applied Sciences, now known as Tampere University of Applied Sciences. The study was done with the approval of the ethical committee of Tampere University Hospital, Tampere, and each participant gave a written informed consent.

In accordance with previous classification scheme [62; 63], the athletes were grouped into five different exercise-loading types: (I) high-impact (H-I) exercise-loading group, (II) odd-impact (O-I) exercise-loading group, (III) high-magnitude (H-M) exercise-loading group, (IV) repetitive, low-impact (L-I) exercise-loading group and (V) non-impact (N-I) exercise-loading group. The high-impact exercise-loading group comprised the triple-jumpers and high-jumpers (22.3 ± 4.1 yrs.); the odd-impact exercise-loading group comprised soccer and squash players (25.3 ± 6.7 yrs.); the high-magnitude exercise-loading group consisted of the power-lifters (27.5 ± 6.3 yrs.); the repetitive, low-impact exercise-loading group constituted the endurance runners (28.9 ± 5.6 yrs.); and the repetitive, non-impact exercise-loading group the swimmers (19.7 ± 2.4 yrs.). The non-athlete group (23.7 ± 3.8 yrs) was used as a referent (REF). All the data are presented as Mean±SD.

4.2. MR image acquisition

The acquisition of MRI images for this study was performed using a 1.5T MRI scanner (Siemens, Avanto, Version Syngo MR B15, Erlangen, Germany). During the process, sagittal, axial and coronal scout images of the pelvic region of the left hip were first obtained using two localization series. Using these scout images as guidance, the imaging plane orientation of the proximal femur was set perpendicular to the femoral neck axis as shown in Figure 4.1. For each subject, muscles attached to the proximal femur region starting from the femoral caput to the subtrochanteric level of the femoral diaphysis were imaged to obtain a total of 120 image slices.

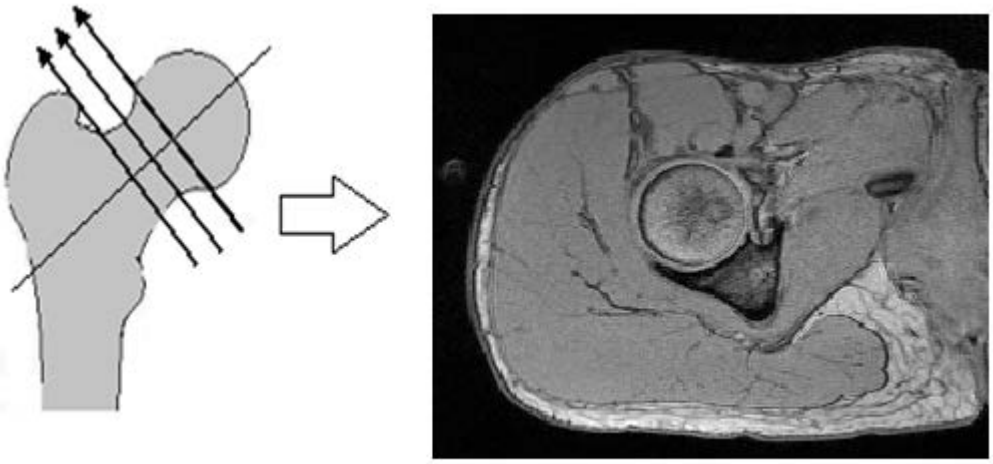

Figure 4.1. *Imaging plan Orientation setup during the MR image acquisition process*

An axial 3D T_1-weighted FLASH (First Low Angle Shot) sequence with interpolation in slice direction was used for this study protocol. The settings of the image acquisition parameters were as follows: repetition time (TR) 15.3 ms, echo time (TE) 3.32 ms, slice thickness 1.00 mm without gaps, pixel size 0.91 mm x 0.91 mm, flip angle of 10° and scan time of 5 minutes. Body matrix coil was used in combination with three elements of spine matrix coil. Normalization filter was also used in order to correct the coil sensitivity profile and to minimize inhomogeneities in the image intensity.

Muscles attached to the proximal femur (hip) that are involved in specific load-bearing during different exercises constituted the anatomical region of interest for texture analysis on this study. The quality of the acquired images was assessed by two radiologists with over ten years of experience and was verified to be of uniform and good quality.

4.3. Slice Selection

The acquired images were exported to Siemens multimodality workplace (Syngo MMWP VE36A, Siemens, Germany) and with the help of the scout images, a reference slice was manually chosen for each subject. As depicted in Figure 4.2 below, the center of the proximal femur caput at the level of articulation capsule insertion was chosen as the reference and the corresponding slice was chosen as the central or reference slice.

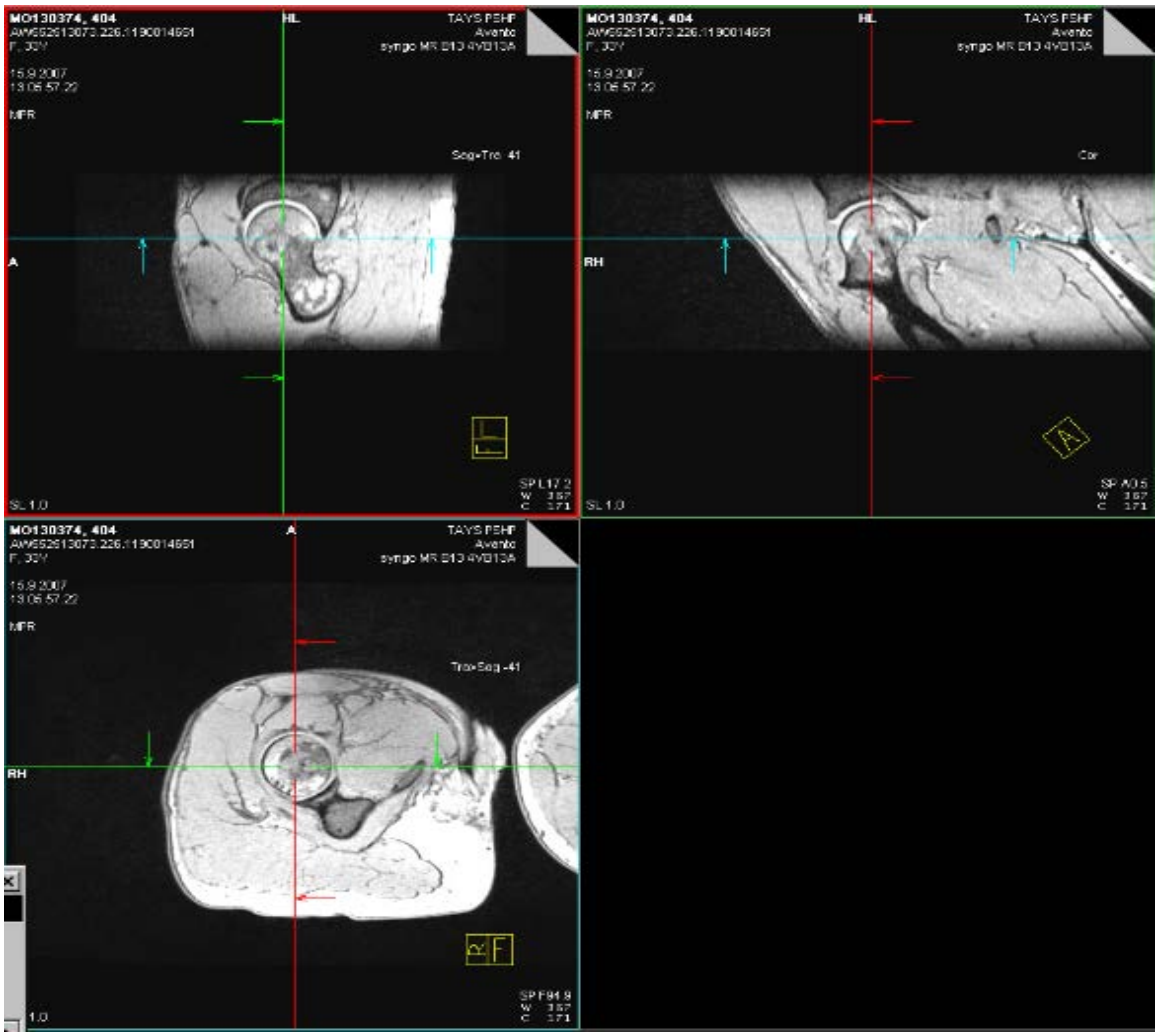

Figure 4.2. *Reference slice selection setup using Siemens Multimodality Workplace*

From the reference slice, five slices were copied from above and below making a total of eleven slices. The images were then converted into DICOM format using Osiris software (Windows version 4.19, The Digital Unit of the Service for Medical Computing of the University Hospital of Geneva, Switzerland) for the texture analysis.

4.4. Texture analysis

Four muscles of the hip region namely; Gluteus maximus, Gluteus medius, Iliopsoas and Obturator internus were chosen for analysis. These muscles were chosen for the quality of research purposes and from biomechanical points of view. From the perspective of research quality, these muscles can be easily distinguished by anatomical landmarks and they also have enough volume for region of interest (ROI) selection to avoid partial volume effect or signals from adjacent tissues so as to get reliable results. The biomechanical and most important reason is based on the specific functionality of each of these muscles in association with load-bearing during different exercises.

To compute texture parameters of these muscles, the selected image slices were first uploaded into texture analysis application software – MaZda (4.6) [64]. In the reference slice of each subject, one homogenous ROI of about 120 pixels (11 x 11) was carefully chosen in each of the four muscles mentioned above for 2D TA analysis. Figure 4.2 below shows the placement of ROIs in the selected muscles. The ROIs were named as Gmax, Gmed, Iliop and ObtInt respectively. In the 3D texture analysis, the same homogeneous region was maintained over ten additional neighboring slices from the reference slice (five up and five below) to form a cubic volume of interest (VOI) of about 1330 voxels in each muscle and in each subject.

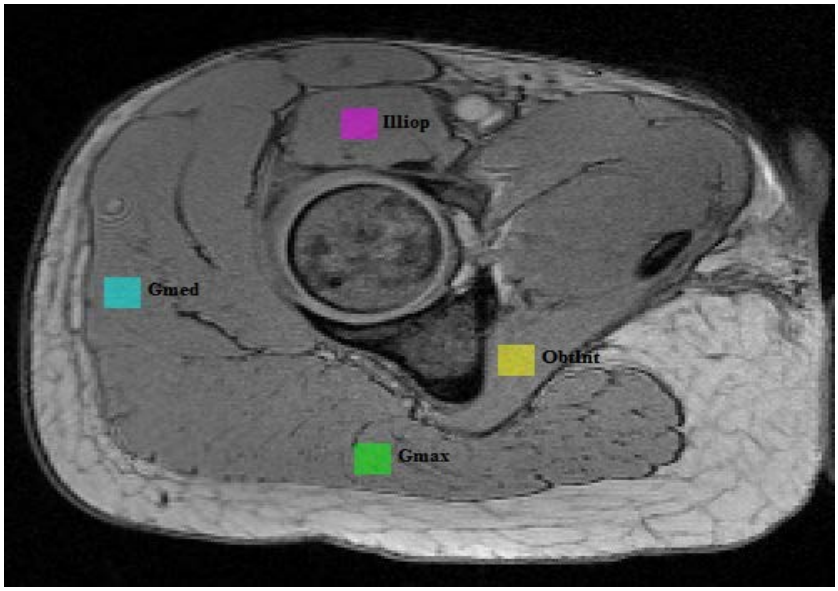

Figure 4.2. *Selected regions of interest (ROIs) in muscles Gluteus maximus (Gmax: blue), Gluteus medius (Gmed: green), Iliopsoas (Iliop: pink) and Obturator internus (ObtInt: yellow)*

The MaZda software was then used to automatically compute texture parameters in each ROI and VOI based on three texture analysis methods: first and second order statistical methods (histogram, co-occurrence matrix, gradient matrix, run-length matrix), transform methods (wavelets) and model-based methods (autoregressive model). In both 2D and 3D, the parameters of co-occurrence matrix were computed for five distances between pixels ($d = 1, 2, 3, 4\ and\ 5$) and in four directions (θ $(0°, 45°, 90°\ and\ 135°)$, and those of the run-length matrix in four directions: horizontal (Horzl_), vertical (Vertl_), slanted at 45 degrees (45dgr_) and slanted at 135 degrees (135dgr_).

In order to shorten computational time and to avoid sparse matrices, the number of grey levels of each ROI and VOI were normalized by restricting their grey level intensities within the range $[\mu - 3\sigma, \mu + 3\sigma]$, where μ is the mean grey level value and σ denotes the standard deviation of each ROI and VOI. Both μ and σ are calculated separately for every ROI and every VOI. A total of about 282 texture features or

parameters were computed for each ROI in 2D and 862 for each VOI in 3D for every subject

4.5. Statistical analysis

The computed texture parameters were converted into excel format for statistical analysis using MATLAB (windows version 7.70, The MathWorks Inc. Natick, Massachusetts, USA) (Refer to appendix 1 for algorithm). For the sake of statistical computational purposes, the ROIs or VOIs – Gmax, Gmed, Iliop and ObtInt were labeled as 1, 2, 3 and 4 respectively whereas the athlete groups – high-impact (H-I), odd-impact (O-I), high-magnitude (H-M), low-impact (L-I) and non-impact (N-I) exercise-loading groups were assigned variable values of 100, 200, 300, 400 and 500 respectively. The non-athlete (REF) group was labeled as 600.

4.5.1. Feature selection and reduction

Since the data set was very huge, there was the need to exclude invariant parameters that do not carry important image information. Hence, among the large number of computed parameters based on the three texture analysis methods mentioned above, only parameters that showed high discriminatory potential for classification and separation between any of the two muscles or between the non-athlete group and any of the athlete groups were selected for further statistical analysis. These parameters were selected by calculating Fisher coefficient (F) – the ratio between-class variance and within-class variance, keeping only the first ten parameters with the highest Fs. These parameters were termed as “discriminant parameters”. SPSS (Windows version 20.0.0; SPSS, Chicago, Ill.) was used in this computation.

According to the rule mentioned above, texture features that served as good discriminators between any of the two muscles were selected as “discriminant parameters” for comparing those muscles. There were six possible comparisons (muscle pairs) between the four muscles. Hence, six sets of discriminant parameters (10 in each set) were selected.

In the group analysis however, the main objective was to compare the athletes groups against the non-athlete (REF) group. Therefore, the discriminant parameters for comparing the groups were selected by choosing texture features that highly discriminate between the non-athlete group (REF) and any other athlete group. In this comparison, there were five possible group pairs, therefore, five sets of discriminant parameters (10 in each set) were selected.

The parameter selection process was done separately for 2D and 3D texture parameters. In order to reduce the effect of noise, the selection of co-occurrence matrix parameters for analysis was limited to a maximum distance (d) of 3 pixels.

4.5.2. Comparison of studied Muscles

The selected discriminant parameters of the muscles were further analyzed statistically using SPSS to examine how the four muscles Gluteus maximus, Gluteus medius, Iliopsoas and Obturator internus differ from each other in terms of texture as result of their functionality differences in load-bearing during different exercises. Nonparametric statistical approach was chosen for this comparison due to the skewed distributions of texture parameters.

Kruskal-Willis test was first used to assess whether statistically significant differences exist among these muscles in general. If affirmed, Mann-Whitney post hoc U test was then performed to ascertain which specific pairs of muscles differed from each other. Because there were six possible comparisons between the muscles, the standard alpha or significance level ($\alpha = 0.05$) was divided by 6 to give 0.00833. Therefore, any p-value less than 0.00833 ($p < 0.00833$) were taken as adequately significant to indicate overall and specific differences between the muscles for both Kruskal-Willis and Mann-Whitney post hoc tests respectively.

In the Kruskal-Willis test, the discriminant parameters from all the muscle pairs were used. If a parameter appeared more than once, only one is taken. However, in the Mann-Whitney test for significant difference between a specific pair of muscles, only the selected set of discriminant parameters for that particular muscle pair were used.

Finally, to further support the findings above, the selected discriminant parameters were used to classify or characterize the muscles by means of linear discriminant analysis (LDA) to find out if the muscles can be separated from each other. The classifications were done using both 2D and 3D texture parameters using SPSS.

4.5.3. Comparison of studied groups

The six study groups were compared and classified just as described above to establish possible differences between non-athlete group and the athlete groups in terms of muscle texture. Since the prime objective of the group analysis was to find out whether the exercise loading or athlete groups differed from the non-athlete group, only Mann-Whitney post hoc U test was performed. Hence, a less stringent p-value ($p < 0.01$) was considered as statistically significant to ascertain that significant differences exist between the referent group and any other athlete group.

4.5.4. Comparative evaluation of 2D and 3D texture analyses

The effectiveness of 2D and 3D TA in detecting and characterizing textural differences were also compared in this work. For every muscle or group pair comparison, the number of 2D discriminant parameters that showed significant differences was compared to those the 3D. Percentages of 2D classification accuracy in showing inter-muscle and inter-group separation were also compared with their corresponding 3D results.

5. RESULTS

Following the methods described above, the results of this work were categorized into three: texture comparison between the studied muscles, comparison between studied groups and comparing the effectiveness of 2D and 3D texture analyses in giving detailed information.

The first results comprise comparison and classification between the four muscles in terms of textural differences. The second part includes comparison and classification between the athlete groups and the non-athlete groups. In each of the instance above, the comparisons and classifications were made separately using 2D and 3D texture parameters. The final part of the results constitutes assessing the abilities of the two texture analyses methods (2D and 3D) to detect and characterize textural differences.

5.1. Comparison of studied muscles

As mentioned above, the results presented in this section include results when the four muscles were compared (test for significant differences in texture) and classified using both 2D and 3D texture parameters. Table 5.1 below shows the sets of discriminant parameters for comparing the muscles.

Table 5.1. *Selected discriminant parameters for respective muscle pair comparison. Refer to Figure 5.1 below for explanation of texture parameters*

Muscle pair	2D discriminant parameters	Fisher's coefficients	3D discriminant parameters	Fisher's coefficients
Gmax vs. Gmed	Perc.01%	99.582	GrSkewness	188.090
	Skewness	93.810	Perc.01%3D	128.876
	S(0,2)SumEntrp	87.810	S(1,-1,1)DifEntrp	108.686
	S(1,-1)DifEntrp	84.704	S(0,1,0)SumOfSqs	98.657
	GrSkewness	80.629	S(0,2,0)SumOfSqs	97.087
	Vertl_GLevNonU	79.050	S(0,0,3)SumEntrp	96.286
	S(0,3)DifEntrp	78.133	S(3,0,-3)SumEntrp	94.923
	S(0,3)SumEntrp	74.499	S(1,-1,0)DifEntrp	92.904
	45dgr_GLevNonU	72.799	S(0,0,2)SumEntrp	92.065
	MinNorm	72.062	S(0,3,0)SumOfSqs	90.678
Gmax vs. Iliop	Vertl_GLevNonU	235.274	S(2,2,0)DifEntrp	285.844
	45dgr_GLevNonU	222.146	S(0,2,-2)DifEntrp	282.653
	135dr_GLevNonU	215.529	S(2,-2,0)DifEntrp	262.398
	Horzl_GLevNonU	215.401	S(0,3,0)DifEntrp	262.064
	S(0,3)DifEntrp	205.533	S(0,3,-3)DifEntrp	261.993
	S(2,-2)DifEntrp	190.126	S(2,-2,-2)DifEntrp	260.221
	S(1,0)DifEntrp	185.844	S(2,-2,2)DifEntrp	258.874
	S(2,2)DifEntrp	182.875	S(1,-1,1)DifEntrp	256.902

	S(2,0)DifEntrp	181.601	S(3,0,0)DifEntrp	254.230
	S(0,3)SumEntrp	176.012	S(2,2,-2)DifEntrp	253.023
	Skewness	100.523	S(0,0,1)Correlat	202.056
	GrSkewness	44.309	S(0,0,1)Contrast	177.790
	Perc.01%	33.898	S(0,0,2)Correlat	165.550
	GrVariance	31.120	S(0,0,1)DifEntrp	155.272
Gmax vs. ObtInt	Kurtosis	27.102	S(0,0,1)DifVarnc	152.830
	S(1,1)DifVarnc	26.124	S(0,0,2)SumVarnc	150.074
	S(1,0)SumOfSqs	22.984	S(0,0,2)Contrast	123.225
	S(2,0)SumOfSqs	19.038	S(0,0,1)InvDfMom	119.930
	S(1,1)SumVarnc	18.340	S(1,-1,1)DifVarnc	108.258
	S(1,0)SumVarnc	17.402	S(0,0,2)DifEntrp	106.885
	Perc.50%	115.197	MaxNorm3D	102.488
	Perc.90%	113.411	MinNorm3D	85.252
	Mean	112.384	Perc.01%3D	58.215
	MaxNorm	108.841	S(2,0,2)Correlat	45.675
Gmed vs. Iliop	Perc.99%	107.443	S(0,2,-2)DifVarnc	41.587
	Perc.10%	98.952	S(2,0,0)DifEntrp	39.964
	MinNorm	74.842	S(2,2,0)Contrast	39.735
	Perc.01%	66.386	S(0,2,-2)Contrast	38.630
	S(2,0)Correlat	57.020	S(2,2,0)DifEntrp	37.542
	S(2,0)SumVarnc	47.020	S(2,0,2)SumVarnc	37.424
	S(1,1)SumEntrp	100.755	S(0,0,1)SumVarnc	179.248
	S(0,1)SumEntrp	94.722	S(0,0,1)DifEntrp	159.042
	S(1,-1)DifEntrp	90.847	S(0,3,-3)SumOfSqs	133.793
	S(0,2)SumEntrp	89.115	S(0,0,2)DifEntrp	131.679
	S(1,-1)SumEntrp	88.327	S(0,2,2)DifEntrp	125.932
Gmed vs. ObtInt	S(2,-2)DifEntrp	87.216	S(2,0,0)SumEntrp	125.821
	S(3,0)DifEntrp	82.285	S(0,1,1)DifEntrp	125.420
	S(2,0)SumEntrp	80.661	S(0,2,-2)SumOfSqs	125.154
	S(0,3)DifEntrp	77.518	S(3,-3,0)DifEntrp	121.226
	S(2,-2)SumEntrp	77.089	S(2,-2,-2)DifEntrp	120.896
	S(2,-2)DifEntrp	274.001	S(0,0,1)DifEntrp	367.562
	S(1,0)DifEntrp	230.726	S(0,2,2)DifEntrp	366.070
	S(3,0)DifEntrp	227.281	S(2,-2,-2)DifEntrp	350.205
	S(1,-1)SumEntrp	219.103	S(0,3,3)DifEntrp	339.355
Iliop vs. ObtInt	S(2,0)DifEntrp	216.553	S(0,0,2)DifEntrp	337.463
	S(3,3)DifEntrp	213.818	S(1,0,-1)DifEntrp	333.442
	S(0,2)DifEntrp	209.993	S(2,0,-2)DifEntrp	332.888
	S(0,3)DifEntrp	198.501	S(3,-3,-3)DifEntrp	332.796
	Vertl_GLevNonU	194.714	S(3,0,0)DifEntrp	322.512
	S(0,1)SumEntrp	193.966	S(2,2,2)DifEntrp	316.869

Figure 5.1 below gives the description of texture parameters. Detailed explanation of these parameters can found in section 3.3

Texture parameter coding/abbreviation	Description
S(x,y,z) DifEntrp	"Difference Entropy" calculated along (x, y, z) direction. E.g. S(1,-1,-1)DifEntrp => Difference Entropy at 1 pixel distance in 135° direction
S(0,2)SumEntrp	"Sum Entropy" calculated along (x, y) direction. E.g. S(0,2)SumEntrp => Sum Entropy at 2 pixel distance in 0° (horizontal) direction
Perc.	Percentile E.g. Perc.99% = 99% percentile
45dgr_GLevNonU	45degrees_Grey Level Nonuniformity
F135dr_LngREmph	135° direction Long Run Emphasis
Vertl_GLevNonU	Vertical Grey Level Nonuniformity
GrNonZeros	Nonzero gradient
F135dr_ShrtREmp	135° direction Long Run Emphasis

Figure 5.1. *Explanation or description of texture parameter coding or abbreviation*

Comparison of studied muscles using 2D texture parameters

Upon performing Kruskal-Willis test using the selected 2D texture parameters, all the tested parameters indicated that significant textural differences ($p - value < 0.00833$) exist among the four muscles in general. The subsequent Mann-Whitney post hoc test also ascertained that each of the four muscles differs significantly from the other. Each texture parameter in the sets of disciriminant parameters used in comparing between all the four muscles (Gluteus maximus and Gluteus medius; Gluteus maximus and Iliopsoas; Gluteus maximus and Obturator internus; Gluteus medius and Iliopsoas; Gluteus medius and Obturator internus, and Iliopsoas and Obturator internus) gave a significant p-value less than 0.00833 as presented in Tables 5.2, 5.3, 5.4, 5.5, 5.6 and 5.7 respectively.

Table 5.2. *Mann-Whitney U Test between gluteus maximus and gluteus medius using 2D texture parameters*

	MinNorm	Skewness	Perc.01%	S(1,-1) DifEntrp	S(0,2) SumEntrp	S(0,3) DifEntrp	S(0,3) SumEntrp	Vertl_ GLevNonU	45dgr_ GLevNonU	GrSkewness
Mann-Whitney U	2707	2033	2162	2278	2244.5	2520	2480	2391	2444	2369
Wilcoxon W	8923	8249	8377.5	8493.5	8461	8734	8696	8607	8660	8585
Z	-7	-9	-8	-8	-8	-8	-8	-8	-8	-8
Asymp. Sig. (2-tailed)	.000	.000	.000	.000	.000	.000	.000	.000	.000	.000

Table 5.3. *Mann-Whitney U Test between gluteus maximus and iliopsoas using 2D texture parameters*

	S(1,0) DifEntrp	S(2,0) DifEntrp	S(2,2) DifEntrp	S(2,-2) DifEntrp	S(0,3) SumEntrp	S(0,3) DifEntrp	Horzl_GLev NonU	Vertl_ GLevNonU	45dgr_ GLevNonU	135dr_ GLevNonU
Mann-Whitney U	1104	1214	1093	1074	1033	992	845	806	782	846
Wilcoxon W	7320	7430	7309	7290	7249	7208	7061	7022	6998	7062
Z	-11	-10	-11	-11	-11	-11	-11	-11	-11	-11
Asymp. Sig. (2-tailed)	.000	.000	.000	.000	.000	.000	.000	.000	.000	.000

Table 5.4. *Mann-Whitney U Test between Gluteus maximus and obturator internus using 2D texture parameters*

	Skewness	Kurtosis	Perc.01%	S(1,0) SumOfSqs	S(1,0) SumVarnc	S(1,1) SumVarnc	S(1,1) DifVarnc	S(2,0) SumOfSqs	Gr Variance	GrSkewness
Mann-Whitney U	1706	2092	3501	3538	4317	4251	3796	3882	3599	2834
Wilcoxon W	7922	8308	9716	9754	10533	10467	10012	10098	9815	9050
Z	-9	-8	-6	-6	-4	-4	-5	-5	-5	-7
Asymp. Sig. (2-tailed)	.000	.000	.000	.000	.000	.000	.000	.000	.000	.000

Table 5.5. *Mann-Whitney U Test texture between Gluteus medius and iliopsoas using 2D texture parameters*

	MinNorm	MaxNorm	Mean	Perc.01%	Perc.10%	Perc.50%	Perc.90%	Perc.99%	S(2,0)Correlat	S(2,0) SumVarnc
Mann-Whitney U	2080	1419	1359	2270	1544	1334	1349	1414	3007	3267
Wilcoxon W	8296	7635	7575	8486	7760	7550	7565	7630	9223	9483
Z	-9	-10	-10	-8	-10	-10	-10	-10	-7	-6
Asymp. Sig. (2-tailed)	.000	.000	.000	.000	.000	.000	.000	.000	.000	.000

Table 5.6. *A Mann-Whitney U Test between Gluteus medius and obturator internus using 2D texture parameters*

	S(0,1) SumEntrp	S(1,1) SumEntrp	S(1,-1) SumEntrp	S(1,-1) DifEntrp	S(2,0) SumEntrp	S(0,2) SumEntrp	S(2,-2) SumEntrp	S(2,-2) DifEntrp	S(3,0) DifEntrp	S(0,3) DifEntrp
Mann-Whitney U	2339	1975	2359.5	2118	2285	2071	2330	2212	2360	2404
Wilcoxon W	8555	8191	8575	8334	8501	8286	8546	8428	8576	8620
Z	-9	-9	-8	-8	-8	-9	-8	-8	-8	-8
Asymp. Sig. (2-tailed)	.000	.000	.000	.000	.000	.000	.000	.000	.000	.000

Table 5.7. *Mann-Whitney U Test between iliopsoas and obturator internus using 2D texture parameters*

	S(1,0) DifEntrp	S(0,1) SumEntrp	S(1,-1) SumEntrp	S(2,0) DifEntrp	S(0,2) DifEntrp	S(2,-2) DifEntrp	S(3,0) DifEntrp	S(0,3) DifEntrp	S(3,3) DifEntrp	Vertl_G LevNonU
Mann-Whitney U	801	965	953	930	927	584	859	859	786	781
Wilcoxon W	7017	7182	7169	7147	7143	6800	7074	7075	7002	6997
Z	-11	-11	-11	-11	-11	-12	-11	-11	-11	-11
Asymp. Sig. (2-tailed)	.000	.000	.000	.000	.000	.000	.000	.000	.000	.000

Classification of studied muscles using 2D texture parameters

The classification results in Table 5.8 shows linear discriminant analysis using 2D texture parameters, distinguishing between the four muscles. In general, a high level of separability was recorded between all four muscles. Gluteus maximus and iliopsoas were the most separable, while gluteus medius and obturator internus were the least distinguishable muscles. The discriminant analysis scatter plot of the centroids of the parameters in Figure 5.2 goes on to further indicate that the muscles are linearly separable from each other.

Table 5.8. *Linear discriminant analysis using 2D texture parameters, classifying muscles gluteus maximus (Gmax) gluteus medius (Gmed), Iliopsoas (Iliop) and Obturator internus (ObtInt)*

Discrimination (number of ROIs)	**Predicted Muscle membership**		**Percentage of original cases correctly classified**
	Gmax	**Gmed**	
Gmax (111)	92	19	
vs.			84.2
Gmed (111)	16	95	
	Gmax	**Iliop**	
Gmax (111)	104	7	
vs.			89.6
Iliop (111)	16	95	
	Gmax	**ObtInt**	
Gmax (111)	90	21	
vs.			85.6
ObtInt (111)	11	100	
	Gmed	**Iliop**	
Gmed (111)	99	12	
vs.			86.9
Iliop (111)	17	94	
	Gmed	**ObtInt**	
Gmed (111)	82	29	
vs.			82.9
ObtInt (111)	9	102	
	Iliop	**ObtInt**	
Iliop (111)	90	21	
vs.			88.3
ObtInt (111)	5	106	

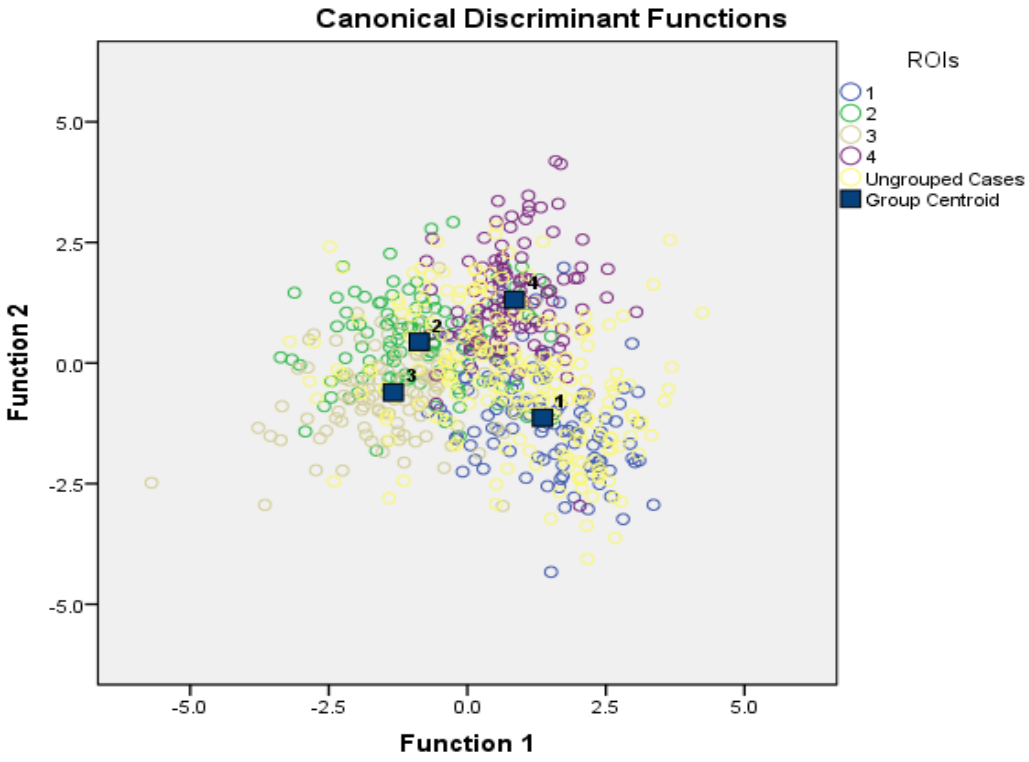

Figure 5.2. *Scatter plot from linear discriminant analysis using 2D texture parameters, separating between muscles: Gluteus maximus (1), Gluteus medius (2), Iliopsoas (3) and Obturator internus (4). Axes function 1 and function 2 represent the discrminant function scores or weights of the individual parameters*

Comparison of studied muscles using 3D texture parameters

Similar to the 2D analysis, all the 3D texture parameters used in the Kruskal-Willis test showed significant differences among the four muscles in a broad-spectrum. This was further affirmed by the subsequent Mann-Whitney post hoc test. As shown in Tables 5.9, 5.10, 5.11, 5.12, 5.13, and 5.14 below, every parameter in the sets of discriminant parameters used in comparing each pair of muscles indicated a significant difference ($p - value \ < \ 0.00833$) between each pair.

Table 5.9. *Mann-Whitney U Test between gluteus maximus and gluteus medius using 3D texture parameters*

	Perc .01%3D	Gr-Skewness	S(0,1,0) SumOfSqs	S(1,-1,0) DifEntrp	S(1,-1,1) DifEntrp	S(0,2,0) SumOfSqs	S(0,0,2) SumEntrp	S(0,3,0) SumOfSqs	S(0,0,3) SumEntrp	S(3,0,-3) SumEntrp
Mann-Whitney U	2497	1229	1754	2076	1781	1728	1932	1978	1944	1967
Wilcoxon W	8713	7445	7970	8292	7997	7944	8148	8194	8160	8183
Z	-9	-10	-9	-9	-9	-9	-9	-9	-9	-8
Asymp. Sig. (2-tailed)	.000	.000	.000	.000	.000	.000	.000	.000	.000	.000

Table 5.10. *Mann-Whitney U Test between gluteus maximus and iliopsoas using 3D texture parameters*

	S(1,-1,1) DifEntrp	S(2,2,0) DifEntrp	S(2,-2,0) DifEntrp	S(2,-2,2) DifEntrp	S(0,2,-2) DifEntrp	S(2,2,-2) DifEntrp	S(2,-2,2) DifEntrp	S(3,0,0) DifEntrp	S(0,3,0) DifEntrp	S(0,3,-3) DifEntrp
Mann-Whitney U	662	570	624	658	556	675	662	672	615	596
Wilcoxon W	6878	6786	6840	6874	6772	6891	6878	6888	6831	6812
Z	-11	-12	-12	-11	-12	-11	-11	-11	-12	-12
Asymp. Sig. (2-tailed)	.000	.000	.000	.000	.000	.000	.000	.000	.000	.000

Table 5.11. *Mann-Whitney U Test between gluteus maximus and obturator internus using 3D texture parameters*

	S(0,0,1) Contrast	S(0,0,1) Correlat	S(0,0,1) InvDfMom	S(0,0,1) DifVarnc	S(0,0,1) DifEntrp	S(1,-1,1) DifVarnc	S(0,0,2) Contrast	S(0,0,2) Correlat	S(0,0,2) SumVarnc	S(0,0,2) DifEntrp
Mann-Whitney U	937	873	1584	1203	1155	2026	1507	1136	1421	1704
Wilcoxon W	7153	7089	7800	7419	7371	8242	7723	7352	7637	7920
Z	-10	-11	-9	-10	-10	-9	-10	-11	-10	-9
Asymp. Sig. (2-tailed)	.000	.000	.000	.000	.000	.000	.000	.000	.000	.000

Table 5.12. *Mann-Whitney U Test between gluteus medius and iliopsoas using 3D texture parameters*

	Min-Norm3D	Max-Norm3D	Perc .01%3D	S(2,0,0) DifEntrp	S(2,2,0) Contrast	S(2,0,2) Correlat	S(2,0,2) SumVarnc	S(2,2,0) DifEntrp	S(0,2,-2) DifVarnc	S(0,2,-2) Contrast
Mann-Whitney U	1922	1453	3552	3091	2928	3264	3443	3165	3039	3192
Wilcoxon W	8138	7669	9768	9307	9144	9480	9659	9381	9255	9408
Z	-9	-10	-7	-6	-7	-6	-7	-6	-6	-6
Asymp. Sig. (2-tailed)	.000	.000	.000	.000	.000	.000	.000	.000	.000	.000

Table 5.13. *Mann-Whitney U Test between gluteus medius and obturator internus using 3D texture parameters*

	S(0,0,1) SumVarnc	S(0,0,1) DifEntrp	S(0,1,1) DifEntrp	S(2,0,0) SumEntrp	S(0,0,2) DifEntrp	S(0,2,2) DifEntrp	S(0,2,-2) SumOfSqs	S(2,-2,-2) DifEntrp	S(3,-3,0) DifEntrp	S(0,3,-3) SumOfSqs
Mann-Whitney U	1188	1479	1580	1497	1624	1740	1646	1707	1797	1489
Wilcoxon W	7404	7695	7796	7713	7840	7956	7862	7923	8013	7705
Z	-10	-10	-10	-10	-9	-9	-9	-9	-9	-10
Asymp. Sig. (2-tailed)	.000	.000	.000	.000	.000	.000	.000	.000	.000	.000

Table 5.14. *Mann-Whitney U Test between iliopsoas and obturator internus using 3D texture parameters*

	S(0,0,1) DifEntrp	S(1,0,-1) DifEntrp	S(0,0,2) DifEntrp	S(2,0,-2) DifEntrp	S(0,2,2) DifEntrp	S(2,2,2) DifEntrp	S(2,-2,2) DifEntrp	S(3,0,0) DifEntrp	S(0,3,3) DifEntrp	S(3,-3,3) DifEntrp
Mann-Whitney U	531	537	533	434	370	446	364	368	341	427
Wilcoxon W	6747	6753	6749	6650	6586	6662	6580	6584	6557	6643
Z	-12	-12	-12	-12	-12	-12	-12	-12	-12	-13
Asymp. Sig. (2-tailed)	.000	.000	.000	.000	.000	.000	.000	.000	.000	.000

Classification of studied muscles using 3D texture parameters

Table 5.15 shows linear discriminant analysis classification of the muscles using 3D texture parameters. Here too, high level of separability was recorded between all the muscles. However, gluteus maximus and obturator internus were the most separable muscles, whereas gluteus medius and iliopsoas were the least. The corresponding discriminant function scatter plot of the parameters in Figure 5.3 also shows that the muscles can be linearly separated from each other.

Table 5.15. *A linear discriminant analysis using 3D texture parameters, classifying between muscles gluteus maximus (Gmax) gluteus medius (Gmed), Iliopsoas (Iliop) and Obturator internus (ObtInt)*

Discrimination (number of VOIs)	**Predicted Muscle membership**		**Percentage of original cases correctly classified**
	Gmax	**Gmed**	
Gmax	97	14	
vs.			89.6
Gmed	9	102	
	Gmax	**Iliop**	
Gmax	103	8	
vs.			89.6
Iliop	15	96	
	Gmax	**ObtInt**	
Gmax	106	5	
vs.			97.3
ObtInt	1	110	
	Gmed	**Iliop**	
Gmed	97	14	
vs.			82.4
Iliop	25	86	
	Gmed	**ObtInt**	
Gmed	103	8	
vs.			93.7
ObtInt	6	105	
	Iliop	**ObtInt**	
Iliop	96	15	
vs.			92.8
ObtInt	1	110	

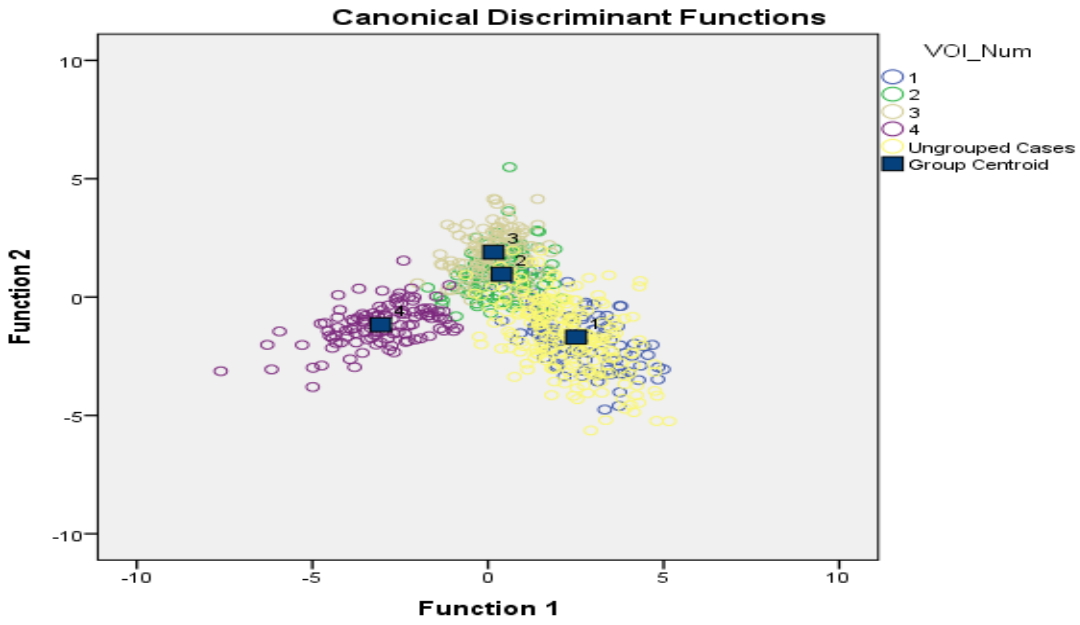

Figure 5.3. *Scatter plot from linear discriminant analysis using 3D texture parameters, separating between muscles: Gluteus maximus (1), Gluteus medius (2), Iliopsoas (3) and Obturator internus (4). Axes function 1 and function 2 represent the discrminant function scores or weights of the individual parameters*

5.2. Comparison of studied groups

Table 5.16 below gives the results of the texture feature reduction and selection processes of selecting discriminant parameters for comparing the athlete groups. These parameters were then used in testing for significant differences and for classifying the athlete groups from the non-athlete group

Table 5.16. *Selected discriminant parameters for respective group pair comparison. Refer to Figure 5.1 for explanation of texture parameter coding or abbreviations*

Group pair	2D Discriminant parameters	Fisher's coefficients	3D Discrimnant parameters	Fisher's coefficients
H-I vs REF	S(2,-2)Contrast	12.263	S(0,2,0)SumVarnc	26.004
	S(2,-2)SumAverg	10.914	S(2,2,0)Correlat	23.432
	S(0,1)Contrast	9.612	S(2,2,0)SumVarnc	22.127
	S(2,-2)SumOfSqs	8.838	S(1,1,0)SumVarnc	20.290
	S(0,2)SumAverg	7.639	S(0,2,0)Correlat	19.607
	S(2,-2)DifVarnc	7.529	S(2,2,2)Correlat	19.559
	S(0,1)DifVarnc	7.490	S(1,1,1)Correlat	19.482
	S(0,1)Correlat	6.952	S(3,3,0)Correlat	18.976
	S(1,-1)SumAverg	6.497	S(1,1,1)DifVarnc	18.569
	S(3,0)Contrast	5.886	S(2,0,0)SumVarnc	18.270

O-I vs REF	S(3,0)SumEntrp	5.041	S(1,0,0)Contrast	14.598
	S(1,0)Correlat	4.725	S(1,0,0)Correlat	14.498
	S(0,1)SumEntrp	4.514	S(1,0,-1)Correlat	12.298
	S(1,0)Contrast	4.245	S(1,0,-1)Contrast	12.091
	S(0,1)SumVarnc	4.093	S(1,0,0)DifVarnc	11.215
	GrNonZeros	3.894	S(1,-1,1)InvDfMom	10.763
	S(1,0)InvDfMom	3.879	S(1,0,-1)DifVarnc	10.706
	GrSkewness	3.631	S(1,0,-1)InvDfMom	9.227
	S(0,1)DifVarnc	3.430	S(1,0,0)SumVarnc	9.145
	S(2,0)AngScMom	3.408	S(1,0,-1)SumVarnc	8.910
H-M vs REF	S(3,3)SumAverg	7.231	S(1,-1,1)InvDfMom	3.596
	S(0,1)Correlat	6.831	S(0,2,2)SumVarnc	3.241
	S(0,1)SumVarnc	6.510	S(1,1,-1)InvDfMom	3.197
	GrNonZeros	6.263	S(3,-3,3)InvDfMom	3.182
	S(0,3)SumAverg	6.028	S(2,-2,-2)SumAverg	3.135
	S(0,2)SumAverg	5.599	S(1,0,-1)DifVarnc	3.092
	S(0,1)Contrast	4.973	S(2,0,-2)Correlat	2.999
	S(2,2)SumAverg	4.850	Perc.50%3D	2.985
	S(2,-2)SumAverg	4.527	S(3,3,0)SumVarnc	2.947
	S(2,2)InvDfMom	3.942	S(0,2,2)Correlat	2.918
L-I vs REF	S(0,1)SumVarnc	8.255	S(2,0,-2)Contrast	22.142
	S(1,0)DifVarnc	6.561	S(2,0,-2)Correlat	21.515
	Kurtosis	6.507	S(2,0,0)Contrast	20.711
	Skewness	5.093	S(1,0,-1)DifVarnc	20.572
	S(1,0)Contrast	4.985	S(2,0,0)Correlat	20.421
	S(0,1)SumOfSqs	4.641	S(2,0,-2)DifVarnc	20.368
	S(3,3)SumAverg	4.433	S(1,0,0)Contrast	19.108
	S(1,0)Correlat	4.324	S(1,0,-1)Contrast	18.959
	S(0,3)SumAverg	4.121	S(1,0,0)Correlat	18.432
	S(2,2)InvDfMom	4.032	S(1,0,0)DifVarnc	17.546
N-I vs REF	S(2,-2)Correlat	7.775	S(1,-1,1)InvDfMom	10.300
	GrNonZeros	5.892	F135dr_LngREmph	8.371
	S(2,-2)Contrast	5.855	F135dr_Fraction	7.762
	S(0,3)Correlat	5.806	S(0,0,1)Contrast	7.466
	S(2,-2)DifVarnc	5.700	F135dr_RLNonUni	7.151
	S(3,0)InvDfMom	5.424	F135dr_ShrtREmp	6.992
	S(2,-2)SumVarnc	4.231	BHorzl_LngREmph	5.793
	S(2,2)InvDfMom	3.698	BHorzl_Fraction	5.746
	S(1,0)Correlat	3.492	S(0,0,2)Contrast	5.708
	S(0,3)SumVarnc	3.230	S(3,0,3)InvDfMom	5.584

Comparison of studied groups using 2D texture parameters

Tables 5.17, 5.18, 5.19, 5.20 and 5.21 show the results of the Mann-Whitney U test between the non-athlete group and the athlete groups. The high-impact (Table 5.17) and high-magnitude (Table 5.18) exercise-loading groups had 7 and 1 parameters indicating significant difference ($p - value < 0.01$ between these two groups and the non-athlete group respectively. Surprisingly, none of the tested discriminant parameters indicated significant difference between the non-athlete group and the odd-impact, low-impact and the non-impact exercise-loading group as shown in Tables 5.19, 5.20 and 5.21 respectively.

Table 5.17. *Mann-Whitney U Test for significant difference between* non-athlete group and high-impact exercise-loading group, *using 2D texture parameters*

	S(0,1) Contrast	S(0,1) Correlat	S(0,1) DifVarnc	S(1,-1) SumAverg	S(0,2) SumAverg	S(2,-2) Contrast	S(2,-2) SumOfSqs	S(2,-2) SumAverg	S(2,-2) DifVarnc	S(3,0) Contrast
Mann-Whitney U	2199	2357	2236	2396	2276	2021	2270	2127	2261	2351
Wilcoxon W	5125	5597	5162	5636	5516	4947	5196	5367	5187	5277
Z	-3	-2	-3	-2	-3	-4	-3	-3	-3	-2
Asymp. Sig. (2-tailed)	.003	.015	.004	.022	.007	.000	.006	.001	.006	.015

Table 5.18. *Mann-Whitney U Test for significant difference between* non-athlete group and high-magnitude exercise-loading group, *using 2D texture parameters*

	S(0,1) Contrast	S(0,1) Correlat	S(0,1) SumVarnc	S(0,2) SumAverg	S(2,2) InvDfMom	S(2,2) SumAverg	S(2,-2) SumAverg	S(0,3) SumAverg	S(3,3) SumAverg	Gr-Variance
Mann-Whitney U	2135	2075	2128	2068	2203	2162	2181	2104	1966	2198
Wilcoxon W	4481	5315	5368	5308	5443	5402	5421	5345	5205	4544
Z	-2	-2	-2	-3	-2	-2	-2	-2	-3	-2
Asymp. Sig. (2-tailed)	.024	.013	.023	.012	.047	.032	.038	.018	.004	.045

Table 5.19. *Mann-Whitney U Test for significant difference between* non-athlete group and odd-impact exercise-loading group, *using 2D texture parameters*

	S(1,0) Contrast	S(1,0) Correlat	S(1,0) InvDfMom	S(0,1) SumVarnc	S(0,1) SumEntrp	S(0,1) DifVarnc	S(2,0) AngScMom	S(2,0) DifEntrp	S(3,0) SumEntrp	Gr-Skewness
Mann-Whitney U	2495	2450	2374	2482	2476	2447	2634	2592	2482	2502
Wilcoxon W	5735	5376	5300	5722	5716	5373	5560	5832	5722	5428
Z	-2	-2	-2	-2	-2	-2	-1	-1	-2	-2
Asymp. Sig. (2-tailed)	.053	.036	.018	.048	.046	.036	.149	.113	.048	.056

Table 5.20. *Mann-Whitney U Test for significant difference between* non-athlete group and low-impact exercise-loading group, *using 2D texture parameters*

	Skewness	Kurtosis	S(1,0) Contrast	S(1,0) Correlat	S(1,0) DifVarnc	S(0,1) SumOfSqs	S(0,1) SumVarnc	S(2,2) InvDfMom	S(0,3) SumAverg	S(3,3) SumAverg
Mann-Whitney U	2505	2546	2297	2355	2218	2462	2207	2342	2295	2255
Wilcoxon W	5745	5174	5537	4983	5458	5702	5447	5582	5535	5495
Z	-1	-1	-2	-2	-2	-2	-2	-2	-2	-2
Asymp. Sig. (2-tailed)	.166	.218	.031	.053	.015	.123	.013	.047	.031	.021

Table 5.21. *Mann-Whitney U Test for significant difference between* non-athlete group and non-impact exercise-loading group, *using 2D texture parameters*

	S(1,0) Contrast	S(1,0) Correlat	S(2,2) InvDfMom	S(2,-2) Contrast	S(2,-2) Correlat	S(2,-2) SumVarnc	S(2,2) DifVarnc	S(3,0) InvDfMom	S(0,3) Correlat	S(0,3) SumVarnc
Mann-Whitney U	2464	2435	2377	2283	2170	2270	2336	2347	2233	2419
Wilcoxon W	5704	5063	5617	4911	5410	5510	4964	4975	5473	5659
Z	-2	-2	-2	-2	-3	-2	-2	-2	-2	-2
Asymp. Sig. (2-tailed)	.125	.101	.063	.028	.009	.024	.045	.049	.017	.089

Classification of studied groups using 2D texture parameters

Table 5.22 below shows the classification results of a linear discriminant analysis discriminating the non-athlete group from the athlete groups when using 2D texture parameters. In general, separability between the groups was not very high. As depicted in Figure 5.4 below, the low-magnitude exercise-loading group was found to be the most separable group from the non-athletes whereas the non-impact exercise-loading group was almost inseparable from the non-athlete group

Since the athlete groups were been separated from a referent group, the concept of sensitivity and specificity was borrowed. The non-athlete group was termed negative and the athlete groups the positives.

Table 5.22. *Linear discriminant analysis using 2D texture parameters, classifying between non-athlete group (REF) and high-impact (H-I), odd-impact group (O-I), high-magnitude (H-M), low-impact (L-I) and non-impact (N-I) exercise-loading groups (TP: True Positive, FP: False Positive, TN: True Negative, FN: False Negative)*

Group classification (Number of ROIs)	TN	FP	TP	FN	S_p (%)	S_v (%)	Original cases Correctly classified (%)
REF (80) vs. H-I (76)	56	24	47	29	70.0	61.8	66.0
REF (80) vs. O-I (76)	56	24	51	25	70.0	67.1	68.6
REF (80) vs. H-M (68)	58	22	41	27	72.5	60.3	66.9
REF (80) vs. L-I (72)	59	21	46	26	73.8	63.9	69.1
REF(80) vs. N-I (72)	55	25	43	29	68.8	59.7	64.5

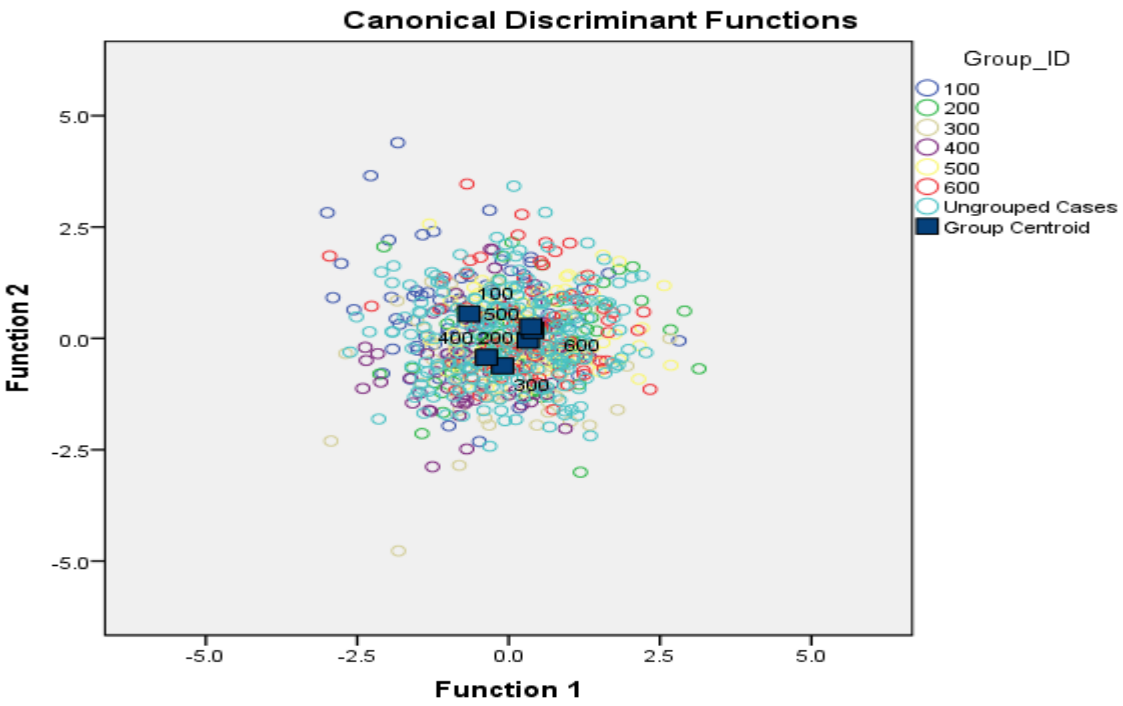

Figure 5.4. *Linear discriminant analysis scatter plot of 2D texture parameters, discriminating between nonathlete group (600) and high-impact (100), odd-impact (200), high-magnitude (300), low-impact (400) and non-impact(500) exercise-loading groups. Axes function 1 and function 2 represent the discrminant function scores or weights of the individual parameters*

Comparison of studied groups using 3D texture parameters

Tables 5.23, 5.24, 5.25, 5.26 and 5.27 show the results of Mann-Whitney U Test for significant differences between the non-athlete group and the high-impact, odd-impact, low-impact, non-impact and the high-magnitude exercise-loading groups respectively. These comparisons were made using texture parameters computed from3D texture analysis. From results, significant differences ($p - value < 0.01$) were found between the non-athlete group and the high-impact, odd-impact and low-impact exercise-loading groups

Also, as depicted in Table 5.26 below, significant differences were recorded in five out of the ten discriminant parameters used in comparing the non-athlete group and the non-impact exercise-loading group. On the contrary, no significant difference was recorded between the non-athletes and the high-magnitude exercise-loading group (Table 5.27)

Table 5.23. *Mann-Whitney U Test between* non-athlete group and high-impact athlete *group using 3D texture parameters*

	S(1,1,0) SumVarnc	S(1,1,1) Correlat	S(1,1,1) DifVarnc	S(2,0,0) SumVarnc	S(0,2,0) Correlat	S(0,2,0) SumVarnc	S(2,2,0) Correlat	S(2,2,0) SumVarnc	S(2,2,2) Correlat	S(3,3,0) Correlat
Mann-Whitney U	1879	1783	1858	1905	1922	1725	1888	1851	1825	1908
Wilcoxon W	4805	4709	5098	4831	4848	4651	4814	4777	4751	4834
Z	-4	-4	-4	-4	-4	-5	-4	-4	-4	-4
Asymp. Sig. (2-tailed)	.000	.000	.000	.000	.000	.000	.000	.000	.000	.000

Table 5.24. *Mann-Whitney U Test between non-*athletes *and odd-impact* athletes *using 3D texture parameters*

	S(1,0,0) Contrast	S(1,0,0) Correlat	S(1,0,0) SumVarnc	S(1,0,0) DifVarnc	S(1,-1,1) InvDfMom	S(1,0,-1) Contrast	S(1,0,-1) Correlat	S(1,0,-1) InvDfMom	S(1,0,-1) SumVarnc	S(1,0,-1) DifVarnc
Mann-Whitney U	1930	1955	2112	2132	1962	2118	2130	2095	2292	2185
Wilcoxon W	5170	4881	5038	5372	4888	5358	5056	5021	5218	5425
Z	-4	-4	-3	-3	-4	-3	-3	-3	-3	-3
Asymp. Sig. (2-tailed)	.000	.000	.001	.001	.000	.001	.001	.001	.008	.002

Table 5.25. *Mann-Whitney U Test between* non athletes and low-impact athletes *using 3D texture parameters*

	S(1,0,0) Contrast	S(1,0,0) Correlat	S(1,0,0) DifVarnc	S(1,0,-1) Contrast	S(1,0,-1) DifVarnc	S(2,0,0) Contrast	S(2,0,0) Correlat	S(2,0,-2) Contrast	S(2,0,-2) Correlat	S(2,0,-2) DifVarnc
Mann-Whitney U	1715	1723	1801	1818	1747	1767	1801	1705	1797	1708
Wilcoxon W	4955	4351	5041	5058	4987	5007	4429	4945	4425	4948
Z	-4	-4	-4	-4	-4	-4	-4	-4	-4	-4
Asymp. Sig. (2-tailed)	.000	.000	.000	.000	.000	.000	.000	.000	.000	.000

Table 5.26. *Mann-Whitney U Test for significant difference between non-*athletes and non-impact athletes *using 3D texture parameters*

	S(0,0,1) Contrast	S(1,-1,1) InvDfMom	S(0,0,2) Contrast	S(3,0,3) InvDfMom	F135dr_ RLNonUni	F135dr_ LngREmph	F135dr_ ShrtREmp	F135dr_ Fraction	BHorzl_ LngREmph	BHorzl_ Fraction
Mann-Whitney U	2515	2023	2505	2287	2193	2145	2193	2171	2155	2174
Wilcoxon W	5755	4651	5745	4915	5435	4773	5432	5411	4783	5414
Z	-1	-3	-1	-2	-3	-3	-3	-3	-3	-3
Asymp. Sig. (2-tailed)	.178	.002	.166	.029	.011	.007	.011	.009	.007	.009

Table 5.27. *Mann-Whitney U Test for significant difference between* non-athletes and high-magnitude athletes *using 3D texture parameters*

	Perc .50%3D	**S(1,-1,1) InvDfMom**	**S(1,0,-1) DifVarnc**	**S(1,1,-1) InvDfMom**	**S(0,2,2) Correlat**	**S(0,2,2) SumVarnc**	**S(2,0,-2) Correlat**	**S(2,-2,2) SumAverg**	**S(3,3,0) SumVarnc**	**S(3,-3,3) InvDfMom**
Mann-Whitney U	2556	2061	2313	2251	2311	2288	2351	2387	2386	2402
Wilcoxon W	5796	4407	5553	5491	4657	4634	4697	5627	4732	5642
Z	-2	-3	-2	-2	-2	-2	-1	-1	-1	-1
Asymp. Sig. (2-tailed)	.086	.011	.117	.071	.116	.096	.156	.200	.199	.221

Classification of studied groups using 3D texture parameters

The classification results in Table 5.28 shows linear discriminant analysis using 3D texture parameters, distinguishing the non-athlete group from the athlete groups. Again, the concept of sensitivity and specificity was borrowed. The non-athlete group was termed negative and the athlete groups the positives. Whereas the high-impact exercise-loading group was found to be the most separable from the non-athlete group, the high-magnitude exercise-loading group was nearly inseparable from the non-athlete group. This can be seen from LDA scatter plot of the group centroids illustrated in Figure 5.5.

Table 5.28. *Linear discriminant analysis using 3D texture parameters, classifying non-athlete group (REF) from high-impact (H-I), odd-impact (O-I), high-magnitude (H-M), low-impact (L-I) and non-impact (N-I) exercise-loading groups: (TN: True Negative, FN: False Negative, TP: True Positive, FP: False Positive)*

Group classification (Number of ROIs)	TN	FP	TP	FN	S_p (%)	S_v (%)	Correctly classified cases (%)
REF (80) vs. H-I (76)	52	28	58	18	65.0	76.3	70.5
REF (80) vs. O-I (76)	54	26	53	23	67.5	69.7	68.6
REF (80) vs. H-M (68)	59	21	39	29	73.8	57.4	66.2
REF (80) vs. L-I (72)	53	27	46	26	66.3	63.9	65.1
REF(80) vs. N-I (72)	58	22	44	28	73.0	61.1	67.1

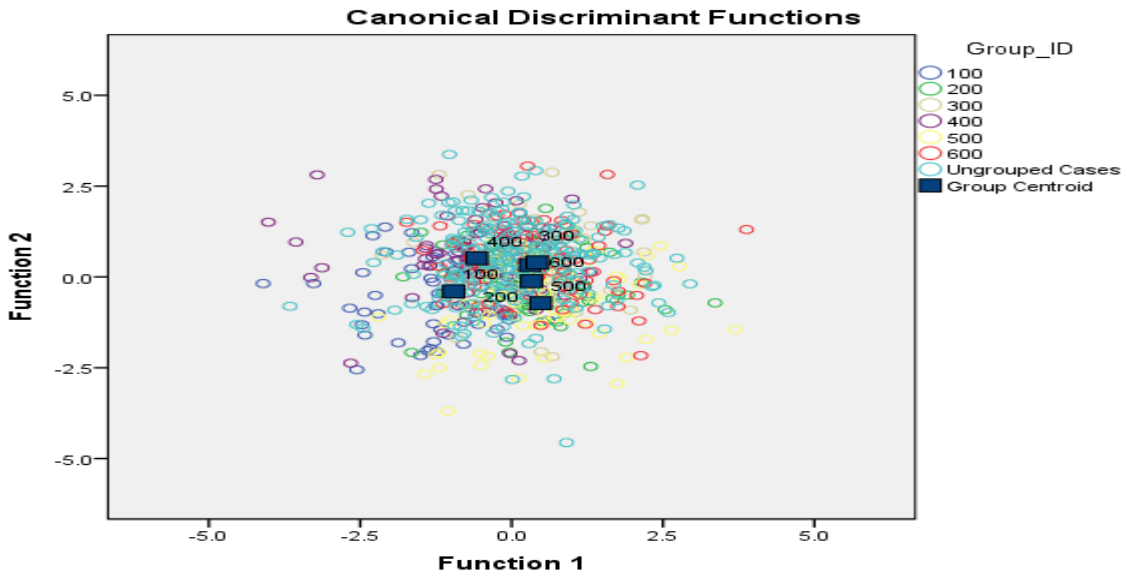

Figure 5.5. *Linear discriminant analysis scatter plot using 3D texture parameters, separating non-athlete group (600) from high-impact (100), odd-impact (200), high-magnitude (300), low-impact (400) and non-impact (500) exercise-loading athlete groups. Axes function 1 and function 2 represent the discrminant function scores or weights of the individual parameters*

5.3. Comparative evaluation of 2D and 3D texture analyses

In terms of revealing significant difference between the muscles, the performances of 2D and 3D texture analyses were the same. Both analyses methods indicated significant differences ($p - value < 0.00833$) between the muscles. However, 3D texture analysis performed better in classifying or separating between the muscles as presented in Figure 5.6.

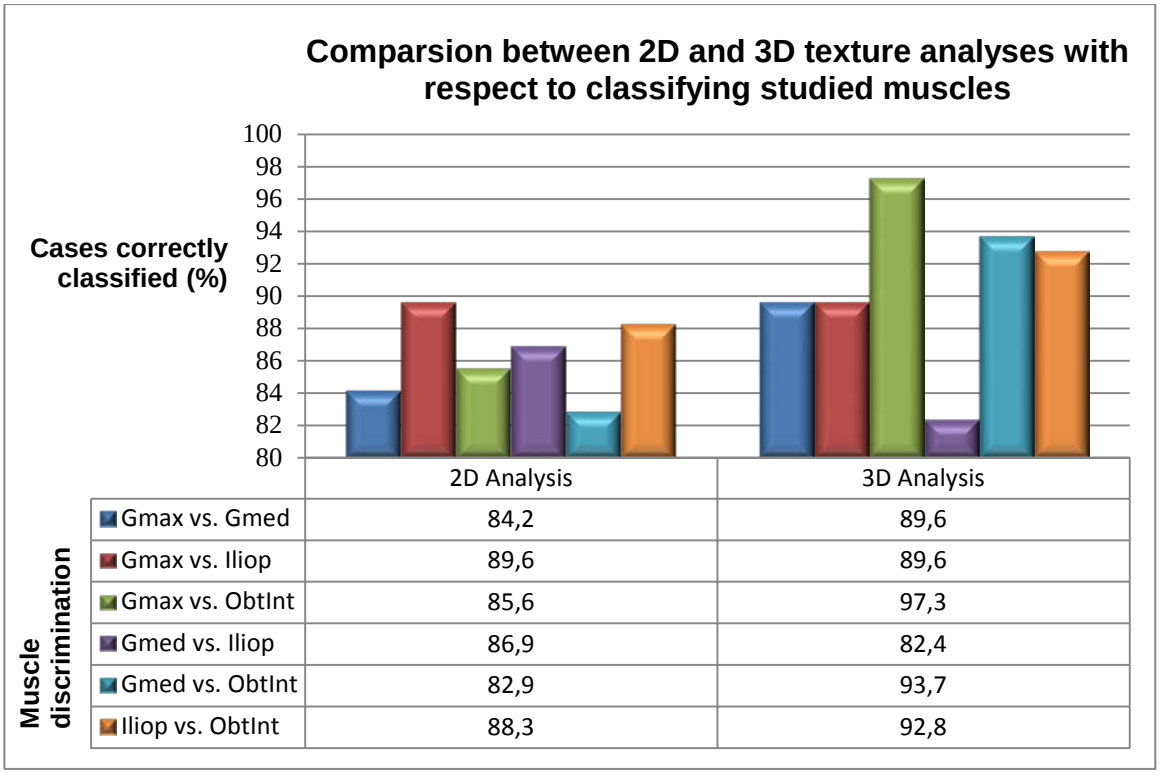

Figure 5.6. A *Comparative classification using 2D and 3D texture parameters between* gluteus maximus, gluteus medius, iliopsoas and obturator internus

With respect to comparing the athlete groups against the non-athlete group, Figure 5.7 shows that 3D texture parameters are more effective in establishing significant difference than 2D parameters. Surprisingly, the performances of the two methods were more or less the same in classifying the groups as depicted in Figure 5.8.

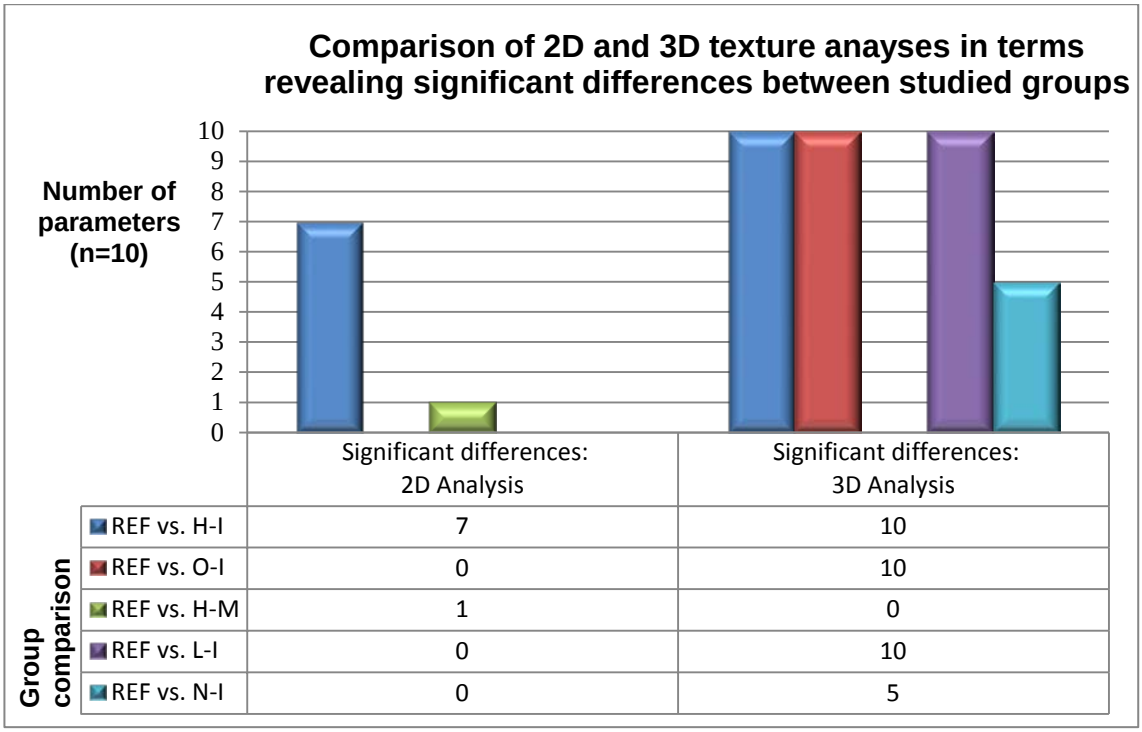

Figure ***Figure 5.7.*** *Comparison of effectiveness of 2D and 3D texture analyses in revealing significance difference between non-athlete and athlete groups*

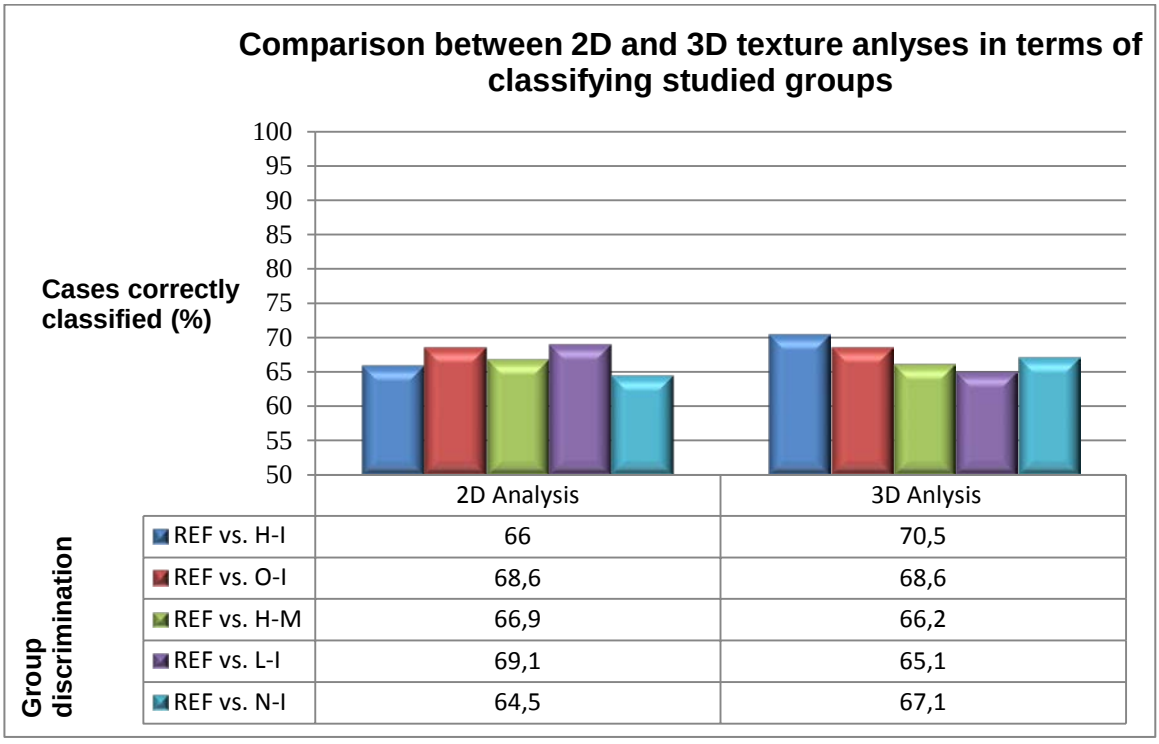

Figure 5.8. A *Comparative classification using 2D and 3D texture parameters between non-athlete and athlete groups*

6. DISCUSSION

This study constitutes part of two major research projects: quantitative analysis of MRI images through texture analysis and monitoring effects of exercise load-associated differences or physical activity on the body. My part of these projects was to assess the ability of texture analysis (TA) to detect textural differences in MR images of skeletal muscles due to exercise load-associated differences.

The superior sensitivity of MRI in detecting subtle changes in soft tissues has made it the imaging modality of choice in most clinical settings. This has led to a number of recent studies on automated analysis of MR images through texture analysis. However, most of these studies have focused on using two-dimensional (2D) texture analysis in detecting and classifying pathological tissues from healthy tissues. There is still the need for further studies in this area especially the dimension of analysis, since 2D is a representation of a single two-dimensional slice of a three-dimensional (3D) structure over an image volume.

In this study, 2D and 3D MRI texture analyses were performed on four hip skeletal muscles (Gluteus maximus, Gluteus medius, Iliopsoas and Obturator internus) of five distinct loading sport groups (high-impact, odd-impact, high-magnitude, low-impact and non-impact exercise-loading) and a healthy non-athlete (referent) group.

Textural differences in the four muscles were compared and the athlete groups were characterized from the non-athlete groups to examine whether exercise load-associated differences in hip muscle texture exist. Finally the study also compared the effectiveness of 2D and 3D texture analyses in detecting and characterizing these textural and loading group differences.

6.1. Comparison of studied muscles

Skeletal muscles are attached to the skeleton. They control skeletal motion and joint movements by providing forces. The amount of force produced by these muscles depends on the muscle fiber cross-sectional area, number of muscles fibers and muscle type [8]. During training or exercise, muscles adapt to the forces or loads they are subjected to, based on the type of exercise or training. This adaptation leads to changes in the size, strength, architecture, structure and mass of the muscles involved [6; 7; 8].

The results (both 2D and 3D) from the comparison between the four study muscles presented in section 5.1 indicate that each of these muscles differs significantly from the other in terms of texture. These differences could be due to the fact that each of these muscles performs different functionalities in load bearing or provision of support to the body. For instance, some previous studies [65; 66; 67; 68; 69] have shown that during running, the gluteus maximus (Gmax) is one of the primary contributors to body support

in forward propulsion (from beginning to mid-stance). The iliopsoas which functions as hip flexor is reported to have minimal contributions to body support and forward propulsion during walking and running but does most of work when a person sits-up. The gluteus medius acts as both thigh extensor and abductor. It provides nearly all the support in mid-stance during walking. The obturator internus is mainly known for lateral rotation of the thigh [10; 65; 68; 70; 71].

These differences in load bearing functionalities can cause corresponding structural and architectural changes or differences in each muscle thereby leading to textural differences in the muscles and hence accounting for the significant differences recorded in the results. The subsequent classification results in Figures 5.2 and 5.3; and in Tables 5.7 and 5.14 also indicate that the four muscles can be linearly separated or distinguished from each other due to differences in their texture. The textural differences in muscle found by this study are consistent with some previous studies [6; 7; 8] which indicated that structural changes occur in skeletal muscles as a result of training or loading.

6.2. Comparison of studied groups

As the results in section 5.2 indicate MRI texture analysis can be used to detect and differentiate apparent exercise-loading group differences in hip muscle texture.

Significant differences in muscle texture were recorded in female athletes who were involved in high-impact (triple-jumpers and high-jumpers), odd-impact (soccer and squash players) and low-impact (endurance runners) exercise-loadings when compared to non-athletes. These findings support the fact that skeletal muscles change in structure and adapt to long term loading or forces acting them. These differences were observed mainly because the kind of loading exercises performed by these athletes differe in comparison to that of non-athletes. Consequently, as expected, muscle texture of these athlete groups differed from the non-athletes. These findings in a way relates to a previous study [72], which recorded significant differences in skeletal muscle architecture between a control group, sprinters and distance runners

On the other hand, very little or no difference was recorded in muscle texture of athletes who participated in high-magnitude (power-lifters) and non-impact (swimmers) exercise-loadings when compared to the non-athlete group. This could partly be due to the fact that the types of exercise-loadings performed by these two athlete groups do not differ much from that of the loading that non-athletes undergo in their daily activities. In view of this, changes in muscle structure and as well as texture are expected not to be different. This result is consistent with previous studies [6; 73]. These studies [6; 73] did not find significant differences between their study athlete groups. They therefore concluded that the loading or movements patterns of the groups were not dissimilar enough to indicate significant differences in muscle structure between the groups.

Finally, the classification results in Tables 5.16 and 5.26, and Figures 5.4 and 5.5 shows there is a separation between the non-athlete group and the athlete groups.

Athletes who performed high-impact odd-impact and low-impact exercise-loadings were linearly (clear-cut) separable from non-athletes. On the other hand, the separation of groups who participated in high-magnitude and non-impact exercise-loadings from non-athletes showed overlapping. Especially, the high-magnitude exercise-loading group was nearly inseparable from the non-athletes. One explanation for this observation could be that movement patterns or impact on hip muscles of power-lifters is very similar to that of non-athletes.

6.3. Comparative evaluation of 2D and 3D texture analyses

Among the texture approaches or numerous image texture descriptors that were used, texture parameters from the second order statistics notably from the co-occurrence matrix were dominant in showing higher discriminatory power between the muscles in both 2D and 3D analyses. In the 2D analysis, texture parameters from the co-occurrence matrix constituted about 60% of the selected “discriminant parameters”, whereas the remaining were made of histogram (first order statistics) and run-length (higher order statistics) parameters. About half of the co-occurrence matrix parameters were ‘difference entropy’ parameters. Similarly, texture parameters from the co-occurrence matrix constituted more than 90% of the discriminant parameters in the 3D analysis; especially ‘difference entropy’ (DifEntrp) texture parameter was outstandingly dominant and the most discriminative parameter.

In both analyses methods, the discrimination between muscles gluteus maximus and iliopsoas, and iliopsoas and obturator internus were mainly dominated by “difference entropy” parameters. Difference entropy measures the randomness of grey level distribution in an image, hence this observation could mean that texture of those muscles is highly random compared to the others. Additionally, the selected discriminant texture parameters for comparing the non-athletes and athletes were all mostly from the co-occurrence matrix parameters for 2D and 3D analyses. However, no particular parameter was exceptionally dominant or common among the group pairs and between the two analyses methods

The ability of the co-occurrence matrix to measure the relative frequency distributions of grey levels and describe how often a particular grey level appears in a specified spatial relationship to another grey level on each image region makes it more sensitive in detecting textural changes in an image, thereby accounting for its higher discriminatory power [59].

It can be deduced from the results presented above that 3D MRI texture analysis is more effective in detecting and characterizing textural differences in skeletal muscles than 2D texture analysis. Although both methods performed equally in the Mann-Whitney U test on the muscles, the 3D method outperformed the 2D in classifying or separating between the muscles (Figure 5.6). Out of the six muscle classifications that were made, 3D texture analysis gave higher classification accuracy in four cases than 2D

except in one case (Gmed vs. Iliop) where the 2D analysis performed slightly better than 3D analysis. Both methods gave equal accuracy result for the classification between gluteus maximus and iliopsoas.

In the athlete groups comparison also (Figure 5.7), 3D texture analysis was able to reveal more significant differences between the groups than the 2D texture analysis. Three-dimensional texture analysis was capable of revealing significant differences between the non-athletes and high-impact, odd-impact and low-impact exercise-loading groups. The 2D analysis however could only indicate significant difference between the non-athletes and the high-impact group.

The effectiveness of 3D texture analysis in detecting and characterizing exercise-loading group differences in hip muscle texture is based on the fact that in 3D TA, textural features are computed from z number of neighboring slices combined into a volume (x, y, and z directions). Therefore a feature that is not captured or present in one slide might be captured or present in the other slices. In 2D however, the computation is made from only one slice in x and y directions. The superiority of 3D texture analysis over 2D in revealing useful clinical information was also reported in previous studies [74; 75] in which various tumors were successfully discriminated from each other and from normal tissues.

6.4. Reliability of results

The use of large sample of athletes representing distinct exercise loadings is the major strength of this study. This large sample size increased the power of the statistical analysis, thereby limiting the chances of committing a type II error.

The precision of texture analysis was verified. Five subjects were randomly chosen from each group and analyzed independently without making reference to the position of ROIs in the original analysis. Upon comparing this result to the original, the same systematic textural differences were recorded between the muscles, even with slight changes in position of the ROIs.

The selected muscles used in the study analysis have enough volume to properly accommodate the RIOs placed in them thereby avoiding partial volume effect or signals from adjacent tissues. In addition, these muscles could be easily and clearly distinguished from one another and other surrounding tissues by anatomical landmarks.

Finally, the reliability of this study is further reinforced by the fact that the conclusions of study were based on two independent statistical analyses methods; non-parametric test (Mann-Whitney U test) and linear discriminant analysis (classification), both of which complement one another.

6.5. Limitations and Recommendations

Despite the numerous strengths of this research, it is not without limitations. The major limitation of this study was the imaging protocol – 1.5T scanner with spatial resolution of 0.9 mm. This was unable to give a much lower resolution within 0.1 – 0.15mm thick of muscle tissue, hence, some microscopic but clinically important textural changes or information was not captured. Therefore, increased imaging resolution might reveal delicate textural details leading to even a better separation of athletes from referents. Another drawback of this study is the positioning of the subjects during the image acquisition process. With the subjects in supine position during the imaging process, the gluteus maximus which constitute most of the buttocks was compressed. This could have affected the structural arrangement muscle fibers or texture in that muscle thereby contributing to the textural differences observed.

The decision on how many parameters to use in the final (statistical) analysis was a major challenge in this study, because, there are no established standards on number of parameters to use. TA analysis computes huge number of textural features such that it is practically impossible to include all of such data in the statistical analysis. The ideal number of parameters to keep during the feature reduction and selection processes needs to be clarified.

There are other interesting and important aspects of this study that needs to be explored futher: In this study, the comparisons between the referent group (non-athletes) and the athlete groups were made in a much broader perspective. In future studies of this kind, it will be more informative to make specific comparsions between the groups with respect a particular muscle. For instance, it will be interesting to find out if texture in the gluteus maximus of odd-impact exerise-loading group differs significantly from that of nonathletes, and the possibility of characterizing them.

Another aspect that will be worth exploring in future studies is the “common discriminant parameters”. During the feature reduction and selection processes, some common parameters were found to show higher discriminatory power between different group or muscle pairs. It could be that these paramaters are more sensitive or contain more textural information, hence the need to concentrate only on these parameters in later studies particularly those from the co-occurrence matrix.

7. CONCLUSION

In this thesis, 2D and 3D MRI texture analyses were carried out on four specific load-bearing hip muscles (Gluteus maximus, Gluteus medius, Iliopsoas and Obturator internus) of five distinct exercise-loading groups (high-impact, odd-impact, high-magnitude, low-impact and non-impact exercise-loading) and a non-athlete (referent) group. Comparisons based on statistical analyses were made to establish differences in texture between the muscles, the athlete groups and the non-athletes, and to classify them accordingly. A comparative evaluation of 2D and 3D texture analyses was then made to determine which of these two dimensions of MRI texture analysis is more effective in detecting and characterizing textural differences.

The four muscles were all found to differ significantly ($p - value < 0.00833$) from each other in terms of texture. The classification of the muscles showed that these muscles are linearly separable. The study also indicated that muscle texture of athletes who participated in high-impact (triple-jumpers and high-jumpers), odd-impact (soccer and squash players) and low-impact (endurance runners) exercise-loadings differ significantly ($p - value < 0.01$) from that of the non-athletes. In addition, the high-impact, odd-impact and low-impact exercise loading groups were completely discriminated (separable) from the non-athlete group. However, muscle texture of the high-magnitude (power lifters) and non-impact (swimmers) exercise-loading groups were not found to differ significantly from that of the non-athletes. The classification of these two athlete groups from the referent group overlapped to some extent. Finally, the 3D texture analysis was more effective in detecting and characterizing textural differences in skeletal muscles than the 2D texture analysis.

In conclusion, 3D texture analysis of MR images provides a more accurate quantitative method for detecting and characterizing textural differences in skeletal muscles that are associated with specific exercise-loading types. However, there is the need for further clinical studies using larger samples to validate these findings.

REFERENCES

[1] Lerski RA., Straughan K., Schad LR., Boyce D., Bluml S. & Zuna I. MR image texture analysis: an approach to tissue characterization. Magn Reson Imag. 11(1993)6, pp. 873–87.

[2] Mir AH., Hanmandlu M. & Tandon SN. Texture analysis of CT. Engineering in Medicine and Biology, IEEE. 14(1995)6, pp. 781 - 786

[3] Skoch A., Jirák D., Vyhnanovská P., Dezortová M., Fendrych P., Rolencová E. & Hájek M. Classification of calf muscle MR images by texture analysis. MAGMA. 16(2004)6, pp. 259-67.

[4] Herlidous S, Rolland Y., Bansard JY., Le Remeur E. & de Certaines JD. Comparison of automated and visual analysis in MRI: characterization of normal and diseased skeletal muscle. Magn Reson Imaging. 17(1999)9, pp. 1393-7

[5] Mahmoud-Ghoneim D., Cherel Y., Lemaire L., de Certaines JD. & Maniere A. Texture analysis of magnetic resonance images of rat muscles during atrophy and regeneration. Magn Reson Imaging. 24(2006) 2, pp. 167-71.

[6] Blazevich AJ., Gill ND., Bronks R. & Newton RU. Training-specific muscle architecture adaptation after 5-wk training in athletes. Med. Sci. Sports Exerc. 35(2003)12, pp. 2013–2022

[7] Baar K., Nader G. & Bodine S. Resistance exercise, muscle loading/unloading and the control of muscle mass. Essays Biochem 42(2006), pp. 61–74

[8] Nakai R., Azuma T., Sudo M., Urayama S., Takizawa O. & Tsutsumi. MRI analysis of structural changes in skeletal muscles and surrounding tissues following long-term walking exercise with training equipment. Journal of Applied Physiology 105(2008)3, pp. 958-963.

[9] Herman Irving P. Physics of the Human Body, 1st ed. Berlin Heidelberg 2007, Springer. 860p.

[10] Seeley RR., Stephens TD. & Tate P. Anatomy and Physiology. 6th ed. Boston 2004, McGraw Hill. 1123p.

[11] Wong LL. Imaging muscle injuries. J HK Coll Radiol. (2005)8, pp. 191–201

[12] Marieb EN. Essentials of Human Anatomy and Physiology. 10th ed. Harlow 2011, Benjamin Cummings. 656p

[13] Bousquet-Santos K., Vaisman M., Barreto ND., Cruz-Filho RA., Salvador BA., Frontera WR. & Nobrega AC. Resistance training improves muscle function and body composition in patients with hyperthyroidism. Arch Phys Med Rehabil 87(2006)8, pp. 1123–1130

[14] Browning RC., Modica JR., Kram R. & Goswami A. The effects of adding mass to the legs on the energetics and biomechanics of walking. Med Sci Sports Exerc 39(2007)3, pp. 515–525

[15] Haddad F. & Adams GR. Aging-sensitive cellular and molecular mechanisms associated with skeletal muscle hypertrophy. J Appl Physiol 100(2006)4, pp. 1188–1203.

[16] Bansal GJ. Digital radiography. A comparison with modern conventional imaging. Postgrad Med J. 82(2006)969, pp. 425-8.

[17] Murphey MD., Quale JL., Martin NL. et al. Computed radiography in musculoskeletal imaging: state of the art. Am J Roentgenol 158(1992)1, pp. 19–27.

[18] Murphey MD. Computed radiography in musculoskeletal imaging. Seminars in Roentgenology 32(1997)1, pp 64-74.

[19] Madge Heath. Digital radiography – the future? Radiography 1(1995)1, pp. 49-60

[20] Kuo GP. & Carrino JA. Skeletal muscle imaging and inflammatory myopathies. Current Opinion in Rheumatology 19(200)6, pp. 530-5.

[21] Guneet Saini. Texture analysis of CT scan images. Master's dissertation, Patiala, 2008, Thapar University, Department of Electrical and Instrumentation. 87p.

[22] Niousha Bolandzadeh-Fasaie. Multi-modal registration of maxillodental CBCT and photogrammetry data over time. Master's dissertation. Edmonton, Alberta, 2011, University of Alberta, Department of Computing Science, 96p.

[23] Sigrid Pillen. Skeletal muscle ultrasound. European Journal Translational Myology 1 (2010) 4, pp. 145-155

[24] Maurits NM., Bollen AE., Windhausen A., De Jager AE. & Van Der Hoeven JH. Muscle ultrasound analysis: normal values and differentiation between myopathies and neuropathies. Ultrasound in Med. & Biol. 29(2003) 2, pp. 215–225

[25] Hajek M., Dezortova M., Materka A. & Lerski R., editors. Texture analysis for magnetic resonance imaging. Prague, Czech Republic 2006, Med4publishing. 233pp.

[26] Westbrook Catherine. MRI at a glnace. Oxford, England 2002, Blackwell Science, 128pp.

[27] Bitar R., Leung G., Perng R. et al. MR Pulse Sequences: what every radiologist wants to know but is afraid to ask. Radiographics 26(2006)2, pp. 513-37.

[28] Holli KK. Texture analysis as a tool for tissue characterization in clinical MRI. Doctorial dissertation. Tampere 2011. Tampere University of Technology, Department of Biomedical Engineering. Publication - Tampere University of Technology, Publication 988. 111p.

[29] Weishaupt D., Kochli V. & Maricek B. How does MRI work: An introduction to the physics and function of magnetic resonance imaging. 2nd ed. Berlin Heidelberg 2006, Springer. 170p.

[30] Nerisho SG. The effect of magnetic resonance imaging sequence on the detection of lymphomas. Master's dissertation. Tampere 2012. Tampere University of Technology, Department of Biomedical Engineering. 59 p.

[31] Kagen LJ. The inflammatory. Ney York 2009, Humana press. 354p.

[32] May DA., Disler DG., Jones EA., Balkissoon AA. & Manaster BJ. Abnormal Signal Intensity in Skeletal Muscle at MR Imaging: Patterns, Pearls, and Pitfalls. Radiographics 20(2000) special issue, pp. 295-315.

[33] Hodler J., Zollikofer Ch. L. & Von Schulthess GK. Musculoskeletal Diseases 200-2012: Diagnostic imaging. Milan Italy 2009, Springer. 256p.

[34] Castellano G., Bonilha L., Li LM. & Cendes F. Texture analysis of medical images. Clinical Radiology 59(2004)12, pp. 1061–1069

[35] Haralick RM., Shanmugam K. & Dinstien I. Textural features for image classification. IEEE Trans Syst Man Cybern. 6(1973), pp. 610 –21

[36] Oliveira MS., Fernandes PT., Avelar WM., Santos SLM., Castellano G. & Li LM. Texture analysis of computed tomography images of acute ischemic stroke patients. Brazilian Journal of Medical and Biological Research 42(2009), pp. 1076-1079

[37] Wilkie JR., Giger ML., Chinander MR., Engh CA., Hopper RH Jr. & Martell JM. Temporal radiographic texture analysis in the detection of periprosthetic osteolysis. Med Phys. 35(2008)1, pp. 377-87

[38] Ahmad M. S., Naweed M. S. & Nisa M. Application of texture analysis in the assessment of chest radiographs. IJVIPNS 9(2009) 9, pp. 291-297

[39] Sakai S., Soeda H., Takahashi N. et al Takahashi N. Computer-aided nodule detection on digital chest radiography: Validation test on consecutive T1 cases of resecTable lung cancer. Journal of Digital Imaging 19 (2006) 4, pp. 376-382.

[40] Ashizawa K., MacMahon H., Ishida T., Nakamura K., Vyborny CJ., Katsuragawa S. & Doi K. Effect of an artificial neural network on radiologists' performance in the differential diagnosis of interstitial lung disease using chest radiographs. Am J Roentgenol. 172(1999)5, pp. 1311-1315.

[41] Mir AH., Hanmandlu M. & Tandon SN. Texture analysis of CT images. IEEE Engineering in Medicine and Biology 14(1995)6, pp. 781-786

[42] Eisele R., Schmid R., Kinzl L., Kramer M., Katzmaier P. & Hartwig E. Soft tissue texture analysis by B-mode ultrasound in the evaluation of impairment in chronic low back pain. European Journal of Ultrasound 8(1998)3, pp. 167–175

[43] Skorton DJ., Collins SM., Nichols J., Pandian NG., Bean JA. & Kerber RE. Quantitative texture analysis in two-dimensional echocardiography: application to the diagnosis of experimental myocardial contusion. Circulation 68(1983)1, pp. 217-23.

[44] Bader W., Böhmer S., van Leeuwen P., Hackmann J., Westhof G. & Hatzmann W. Does texture analysis improve breast ultrasound precision? Ultrasound Obstet Gynecol. 15 (2000)4, pp. 311-316.

[45] Kim N., Amin V., Wilson D., Rouse G. & Udpa S. Ultrasound image texture analysis for characterizing intramuscular fat content of live beef cattle. Ultrasonic Imaging. 20 (1998)3, pp. 191-205

[46] Holli KK., Harrison L., Dastidar P. et al. Texture analysis of MR images of patients with mild traumatic brain injury. BMC Med Imaging. 10 (2010)8, pp. 1-10

[47] Wang L., Li N., Zhou X. & Tong L. Texture Characteristic Analysis of MRI for Exploratory study on early diagnosis of multiple sclerosis. Proceedings of the 2007 IEEE/ICME international conference on complex medical engineering. Beijing, China, May 23-27, 2007. Beijing, 2007, IEEE. pp. 652 – 655.

[48] Harrison LC., Luukkaala T., Pertovaara H. et al. Non-Hodgkin lymphoma response evaluation with MRI texture classification. J Exp Clin Cancer Res. 28 (2009)87

[49] Ojala T. Texture classification. [Online notes]. CVoline. [Accessed on: 09.08.2012]. Available at: http://homepages.inf.ed.ac.uk/rbf/CVonline/LOCAL_COPIES/OJALA1/texclas.htm

[50] Ojala T., Valkealahti K., Oja E. & Pietikäinen M. Texture discrimination with multidimensional distributions of signed grey level differences. Pattern Recogn. 34(2001)3, pp. 727-39

[51] Haralick R. Statistical and structural approaches to texture. IEEE Proceedings 67(1979)5, pp. 786-804

[52] Weszka J., Deya C. & Rosenfeld A. A comparative study of texture measures for terrain classification. IEEE Trans. Systems Man and Cybernetics 6(1976), pp. 269-285

[53] Chen P. & Pavlidis T. Segmentation by texture using a co-occurrence matrix and a split-and merge algorithm. CGIP. 10(1979), pp. 172-182

[54] Argenti F., Alparone L. & Benelli G. Fast algorithms for texture analysis using co-occurrence matrices. IEE Proceedings 137(1990)6, pp. 443-448

[55] Tuceryan M. & Jain AK. Texture Analysis. In: Chen C.H., Pau L.F. & Wang P.S.P. The Handbook of Pattern Recognition and Computer Vision. USA 1998, World Scientific Publishing Co. pp. 207–248.

[56] Pentland AP. Fractal-based description of natural scenes. IEEE Transactions on Pattern Analysis and Machine Intelligence, PAMI-6 (1984)6, pp. 661-674.

[57] Materka A., Strzelecki M. & Szczypiński P. MaZda user's manual. Lodz 2006, Technical University of Lodz, Institute of Electronics. [Accessed 12.08.2012] 83 pp. Available at: http://www.eletel.p.lodz.pl/programy/MaZda/download/MaZda_manual.pdf

[58] Harrison L. Clinical Applicability of MRI Texture Analysis. Doctorial dissertation. Tampere 2011. University of Tampere, School of Medicine. 132p.

[59] Park B. & Chen YR. Co-occurrence Matrix Texture Features of Multi-spectral Images on Poultry Carcasses J. agric. Engng Res. 78(2001)2, pp. 127-139

[60] Mital DP. Autoregressive approach to surface texture analysis. Proceedings IEEE 18th Annual International Conference on Industrial Electronics, Control and Instrumentation, IECON'92, San Diego, California, USA, November 9-13, 1992. California, 1992, IEE. Pp.1309-1312.

[61] Srinivasan GN. & Shobha G. Statistical Texture Analysis. World Academy of Science, Engineering, and Technology 36(2008), pp. 1264-1269.

[62] Harrison LC., Nikander R., Sikio M., et al. MRI texture analysis of femoral neck: Detection of exercise load-associated differences in trabecular bone. JMagn Reson Imaging. 34(2011)6, pp. 1359-99

[63] Nikander R., Kannus P., Dastidar P., et al. Targeted exercise against hip fragility. Osteoporos Int. 20(2009)8, pp. 1321-8

[64] Szczypinski P., Strzelecki M., Materka A., Klepaczko A. MaZda-A software package for image texture analysis, Computer Methods and Programs in Biomedicine, 94(1), 2009, pp. 66-76

[65] Sasaki K., Neptune RR. Differences in muscle function during walking and running at the same speed. J Biomech. 39(2006)11, pp. 2005-13.

[66] Belli A., Kyrolainen H. & Komi PV. Moment and power of lower limb joints in running. Int J Sports Med. 23(2002)2, pp. 136–41.

[67] Simpson KJ., Bates BT. The effects of running speed on lower extremity joint moments generated during the support phase. International Journal of Sport Biomechanics 6(1990) 3, pp. 309–24.

[68] Simonsen EB., Thomsen L. & Klausen K. Activity of mono- and biarticular leg muscles during sprint running. Eur J Appl Physiol Occup Physiol. 54(1985)5, PP. 524–32.

[69] Novacheck TF. Review paper: the biomechanics of running. Gait and Posture 7(1998)1, pp. 77–95.

[70] Anderson FC. & Pandy MG. Individual muscle contributions to support in normal walking. Gait Posture. 17(2003)2, pp. 159-69.

[71] Andersson EA., Nilsson J. & Thorstensson A. Intramuscular EMG from the hip flexor muscles during human locomotion. Acta Physiol Scand. 161(1997)3, pp. 361–370.

[72] Abe T., Kumagai K. & Brechue WF. Muscle fascicle length is greater in sprinters than long distance runners. Med Sci Sports Exerc. 32(2000)6, pp. 1125-9

[73] Sleivert GG., Backus RD. & Wenger HA. The influence of a strength-sprint training sequence on multi-joint power output. Med Sci Sports Exerc. 27(1995)12, pp. 1655-65.

[74] Mahmoud-Ghoneim D., Toussaint G., Constans J. & de Certaines JD. Three-dimensionaltexture analysis in MRI: a preliminary evaluation in gliomas. Magn Reson Imaging. 21(2003)9, pp. 983–7.

[75] Georgiadis P., Cavouras D., Kalatzis I, et al. Enhancing the discrimination accuracy between metastases, gliomas and meningiomas on brain MRI by volumetric textural features and ensemble pattern recognition methods. Magn Reson Imaging. 27(2009)1, pp. 120–30.

APPENDICES

Appendix 1

The MATLAB algorithm used for reading and converting the 2D and 3D output parameters of MaZda software from *.par* format into *excel* format.

```
%% Converting 2D output into excel format
clear all;
close all;
clc;
% Import files %
[filename,myFolder]=uigetfile({'*.par','PAR files(*.par)'},'Choose a .par file','MultiSelect','off');
if ~isdir(myFolder)
errorMessage = sprintf('Error: The following folder does not exist:\n%s', myFolder);
uiwait(warndlg(errorMessage));
return;
end
filePattern = fullfile(myFolder, '*.par');
parFiles = dir(filePattern);
for k = 1:length(parFiles)
baseFileName = parFiles(k).name;
fullFileName = fullfile(myFolder, baseFileName);
fprintf(1, 'Now reading %s\n', fullFileName);
fid = importdata(fullFileName);
% Write columns to vectors column1, column2.... %
column1 = fid.textdata(25:end,1);
column2 = fid.data(:,1);
column3 = fid.data(:,2);
column4 = fid.data(:,3);
column5 = fid.data(:,4);
column6 = fid.data(:,5);
column7 = fid.data(:,6);
% Save to excel file %
[p, baseFileName, e] = fileparts(baseFileName);
file = fullfile(myFolder, baseFileName);
xlswrite(file, column1, 1, 'D1');
xlswrite(file, column2, 1, 'E1');
xlswrite(file, column3, 1, 'F1');
xlswrite(file, column4, 1, 'G1');
xlswrite(file, column5, 1, 'H1');
xlswrite(file, column6, 1, 'I1');
xlswrite(file, column7, 1, 'J1');
drawnow; % Force display to update immediately.
end
disp('Process Complete')    %%% END %%%


%% converting 3D output of into excel format
clear all;
```

```
close all;
clc;
% Import files %
[filename,myFolder]=uigetfile({'*.par','PAR files(*.par)'},'Choose a .par file','MultiSelect','off');
if ~isdir(myFolder)
errorMessage = sprintf('Error: The following folder does not exist:\n%s', myFolder);
uiwait(warndlg(errorMessage));
return;
end
filePattern = fullfile(myFolder, '*.par');
parFiles = dir(filePattern);
for k = 1:length(parFiles)
baseFileName = parFiles(k).name;
fullFileName = fullfile(myFolder, baseFileName);
fprintf(1, 'Now reading %s\n', fullFileName);
fid = importdata(fullFileName);
% write columns to vectors column1, column2.... %
column1 = fid.textdata(14:end,1);
column2 = fid.data(:,1);
column3 = fid.data(:,2);
column4 = fid.data(:,3);
column5 = fid.data(:,4);
column6 = fid.data(:,5);
column7 = fid.data(:,6);
% Save to excel file %
[p, baseFileName, e] = fileparts(baseFileName);
file = fullfile(myFolder, baseFileName);
xlswrite(file, column1, 1, 'D1');
xlswrite(file, column2, 1, 'E1');
xlswrite(file, column3, 1, 'F1');
xlswrite(file, column4, 1, 'G1');
xlswrite(file, column5, 1, 'H1');
xlswrite(file, column6, 1, 'I1');
xlswrite(file, column7, 1, 'J1');
drawnow; % Force display to update immediately.
end
disp('Process Complete')

%%% END %%%
```